A HELIUM MAGNETOMETER THAT UTILIZES LIGHT-MODULATION

ROBERT G. ALDRICH

LIBRARY
U.S. NAVAL POSTGRADUATE SCHOOL
MONTEREY, CALIFORNIA

FEB 20 1961

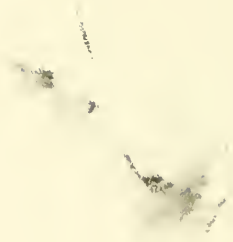

A HELIUM MAGNETOMETER THAT UTILIZES LIGHT-MODULATION

* * * *

Robert G. Aldrich

A HELIUM MAGNETOMETER THAT UTILIZES LIGHT-MODULATION

by

Robert G. Aldrich
Lieutenant Commander, United States Navy

Submitted in partial fulfillment of
the requirements for the degree of

MASTER OF SCIENCE
IN
ENGINEERING ELECTRONICS

United States Naval Postgraduate School
Monterey, California

1 9 6 1

Library
U. S. Naval Postgraduate School
Monterey, California

A HELIUM MAGNETOMETER THAT UTILIZES LIGHT-MODULATION

by

Robert G. Aldrich

This work is accepted as fulfilling
the thesis requirements for the degree of
MASTER OF SCIENCE
IN
ENGINEERING ELECTRONICS
from the
United States Naval Postgraduate School

ABSTRACT

The detection of the Zeeman effect by spin precession experiments has led to the development of magnetometers which utilize vapor or gaseous sensing devices capable of high precision. A recent example of this type of instrument is the helium gas magnetometer. The purpose of this paper is to present the background theory of a helium magnetometer which utilizes a modulated pumping light, and to describe the equipment used to construct an experimental magnetometer system. The feasibility of this system as an instrument to measure changes in the earth's magnetic field is confirmed by comparison with a commercial magnetometer.

The author's work on this device was accomplished at the Varian Associates research laboratory at Palo Alto, California, during the period January to March, 1961.

The author wishes to express his appreciation for the assistance and encouragement given him by Drs. A. L. Bloom and W. E. Bell of Varian Associates during this period.

TABLE OF CONTENTS

Section	Title	Page
I.	Introduction	1
II.	Theoretical Background	4
	A. The Helium Energy Levels	4
	The Field-Free Spectrum	4
	The Zeeman Splitting	7
	The Transitions	9
	The Larmor Precession Process	11
	B. The Signal Development	13
	The Pumping Process	13
	The Phenomological Approach	17
	The Optical Modulation	20
	The Line Shape	24
III.	The Theoretical Magnetometer System	26
	A. General Design	26
	B. The Consideration of Noise	29
IV.	The Experimental Magnetometer System	33
	A. Principles of Construction	33
	B. The System Description	34
V.	The Experimental System Performance	41
	A. The Measurements of the Magnetic Field	41
	B. The Subsidiary Measurements	50
	The Absorption Phenomena	50
	The Signal Processing	53
	The Measurement of Line Width	54
VI.	Conclusions	55
	A. System Performance	55
	Bibliography	58
	Appendix	
A.	Zeeman Level Energy Considerations	59
B.	The Effect of Polarization on Transitions	62
C.	The Population Density Considerations	66
D.	The Equipment Schematic Diagrams	70

LIST OF ILLUSTRATIONS

Figure		Page
1.	The Helium Spin Alignment	5
2.	The Orthohelium Angular Momentum	5
3.	The Helium ^3S State Angular Momentum	5
4.	Helium Spectrum in the Absence of Magnetic Field	6
5.	Helium Energy Levels Showing Zeeman Splitting	8
6.	Fixed Reference Frame	13
7.	The Precessional Reference Frames with Modulated Light	14
8.	Expectation Position of the Spin Vector in a Rotating Frame	16
9.	The Theoretical Magnetometer System	26
10.	Phase Detector Operation when $\omega = \gamma H_c$	27
11.	Phase Detector Operation when $\omega \neq \gamma H_c$	28
12.	Signal Processing Chain	29
13.	Phase Detector Waveforms	30
14.	Noise Variations in the Processed Signal	31
15.	The Experimental Magnetometer System	34
16.	The Experimental Magnetometer- Left Hand View	38
17.	The Experimental Magnetometer- Right Hand View	39
18.	The Experimental Magnetometer- Optical Rack Details	40
19.	System Performance- 27 February, 1961	45
20.	System Performance- 4 March, 1961	46
21.	System Performance 5 - 6 March, 1961	47
22.	Large Field Perturbation- Rubidium Magnetometer 6 March , 1961	48

Figure Page

23. Large Field Perturbation-Helium Magnetometer 6 March, 1961 49

24. Equipment Configuration for Absorption Observation 50

25. Detector Voltage Variation-Lamp on, Cell off 52

26. Detector Voltage Variation-Lamp off, Cell off 52

27. The Unprocessed signal 52

28. Unprocessed signal 53

29. Filtered signal 53

30. Processed Signal 53

31. Vector Sum of the Moments and Momenta 60

32. The Allowed Transitions in Helium 67

Table

1. Absorption Transition Rates 67

2. Relative Spontaneous Emission Probabilities 68

3. Spontaneous Emission Probabilities in terms of Absorption Rates 68

Diagram

1. Photodetector Preamplifier 71

2. 1.4 mc. Oscillator and Frequency Control Unit 72

3. 1.4 mc Modulator and 115 mc. Lamp Exciter 73

4. 60 cycle Phase Detector 74

I. Introduction

The utilization of the earth's magnetic field for man's needs can be traced back through many centuries. To further his advantage, man has undertaken study of this phenomena, and it remains one of today's challenging geophysical frontiers. The present-day requirements for sensitive underwater detection devices have increased the need for precise magnetic field measurement. To meet these needs for measurement, a class of instruments has been developed which uses vapor or gas as the detecting substance. The underlying principle of their operation can be summarized as: (a) accurate detection of the Zeeman effect within the working medium and (b) subsequent utilization of this information to form a self-correcting closed loop system. In this manner the exterior magnetic field information may be extracted when desired or on a continuous basis by suitable recording devices. Such magnetometers, utilizing rubidium vapor, are commercially available.

The work with helium gas as a magnetic field detection device has been largely directed towards obtaining usable resonance signals. However, operating magnetometers using helium have been reported.[1,2] The principle of optical pumping, together with resonant mixing of the metastable helium sublevels, provides a means of detecting the magnitude of the Zeeman effect. This action can be visualized as one which allows the pumping light to cause an unbalance in the metastable population densities followed by a redistribution under the control of external electronic devices. Fortunately, this cycle

[1]P. A. Franken and F. D. Colgrove, The Metastable Helium Magnetometer (1)

[2]Magnetometer System for Orientation in Space, Electronics, April 8, 1960, pp. 55

can be detected easily by monitoring the residual pumping light, i.e., the output light which passes through the sample. This output light will contain information concerning the process. Both polarized and unpolarized light are used for this purpose. The unpolarized light causes a different distribution in the population densities from that caused by the polarized light. In the case of polarized light, a net magnetic moment is formed by increasing the density of one sublevel at the expense of the other sublevels involved. As a practical matter, this difference leads to dissimilar physical effects and no detailed comparison will be made here.[3]

The desired information contained in the output light can take several forms depending on the method of operation desired. In the simple detection scheme described above, the output light information will be in the form of a resonance-like amplitude variation which has a peak position that corresponds to the strength of the ambient magnetic field. This variation can be achieved by 1) introducing into the gas a radio frequency field which corresponds to the Larmor precession frequency and then 2) varying the radio frequency or the total magnetic field in a periodic manner. As the changing frequency or magnetic field passes through resonance, a change in the light absorption will take place.

A second method of utilizing the pumping light is found by fixing the applied radio frequency field at the Larmor precession rate and examining the radio frequency content of the output light. It will be found that the output light is modulated at the applied radio frequency and a closed loop oscillator can be formed at the Larmor

[3]For the unpolarized light physics, see F. D. Colgrove and P. A. Franken (2)

precession frequency. Alternately, it is possible to heterodyne two radio frequencies which are within the line width of the Larmor precession frequency and extract a difference frequency from the light for magnetometer purposes.[4]

The magnetometer constructed in the course of this investigation utilized a principle of "optical modulation" or as alternately phrased, "pumping light modulation".[5] This method utilizes a polarized pumping light to change the population densities of the metastable levels and a pumping light modulation at the appropriate Larmor precession frequency. Passing the light through a helium sample results in a net spin orientation within the gas. Detection of this orientation is accomplished by monitoring the pumping light intensity after it passes through the helium sample. The amount of absorption will be altered as the modulation frequency passes through the natural spin precession frequency corresponding to the ambient magnetic field. This latter method was chosen in preference to the previously mentioned methods because the theoretical conception is of recent origin and not necessarily because it is the most desirable as a practical system. It was the intent of this investigation therefore, to show the feasibility of a magnetometer using modulated light and compare its performance with an existing system, in contrast to making a detailed comparison with other possible helium systems.

In order to present the results of these efforts in a comprehensive manner, this thesis contains a brief discussion of the theoretical background as aided by subsidiary proofs contained in the appendices. This is followed by a discussion of the theoretical magnetometer design which subsequently materialized into experimental hardware.

[4] A. L. Bloom & W.E. Bell, Radiofrequency Mixing in Optical Pumping Experiments, to be published.

[5] W. E. Bell & A.L. Bloom (3)

II. Theoretical Background

A. The Helium Energy Levels

1. The Field-free Spectrum

From the viewpoint of classical mechanics, the atomic electron motion can be analyzed in terms of certain assigned parameters. The first of these arises from the motion of the electron in relation to the nucleus and is expressed in terms of the orbital angular momentum which has a magnitude $\frac{h}{2\pi}\sqrt{l(l+1)} \cong \frac{hl}{2\pi}$ where l is the azimuthal quantum number and h is Planck's constant. To a first approximation, this parameter can be applied to a complicated atom by assigning to each electron an individual orbital angular momentum and taking their vector sum to represent the total orbital angular momentum $\frac{h}{2\pi}\sqrt{L(L+1)} \cong \frac{hL}{2\pi}$. Since analysis by quantum mechanics will show that the individual orbital angular momentum can only be oriented in certain discrete directions to one another, the vector sum can only assume certain values, namely, L = 0,1,2,....

In a similar manner, the assumed rotation of the electron around its own axis will result in an electron spin angular momentum, s. This combines with other electron spins to give a resultant $\frac{h}{2\pi}\sqrt{S(S+1)} \cong \frac{hS}{2\pi}$. Again, only certain discrete values are allowed- S taking on the magnitudes $\frac{N}{2}, \frac{N}{2}-1, \text{----} 0$ where N is the total number of electrons.

The total angular momentum can be found by the vector sum of the orbital and spin momenta to form $\frac{h}{2\pi}\sqrt{J(J+1)} \cong \frac{hJ}{2\pi}$, where again, the discrete magnitudes and directions result in the rule: "The vector sum of $\bar{S}$ and $\bar{L}$ is such that the different possible values have integral differences". It shall be considered here that:

$$\bar{J} = \bar{L} + \bar{S}$$

defines the total angular momentum vector in terms of $\frac{h}{2\pi}$.

The helium spectrum is composed of singlet and triplet lines. This duality arises from the two electron spins, since each has a quantum number $s = \frac{1}{2}$ and they can be aligned parallel or antiparallel. As a result, the spin angular momentum can be zero or one:

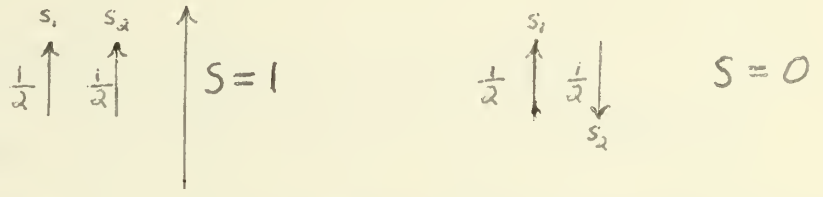

Fig. 1. The Helium Spin Alignment

For the S = 0 combination of electron spins, only singlet lines can appear, and the result is designated parahelium. For example, the P (L = 1) state results in a total angular momentum J = 1 since S = 0 and only one P state per n quantum number will appear.

Orthohelium is the result when S = 1, for then additional energy levels can appear. For the P state (L = 1) three lines will result:

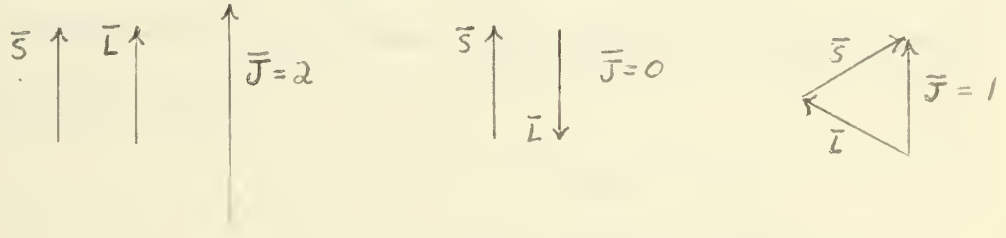

Fig. 2. The Orthohelium Angular Momentum

Also for the orthohelium S state (L = 0):

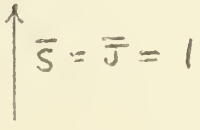

Fig. 3. The Helium ^{3}S State Angular Momentum

The general quantum selection rules for transitions from one state to another are:

a. $\Delta l = \pm 1$

b. $\Delta L = \pm 1, 0$

c. $\Delta S = 0$

d. $\Delta J = \pm 1, 0$ [not $J=0$ to $J=0$]

e. $\Delta M = \pm 1, 0$ [not $M=0$ to $M=0$ if $\Delta J = 0$]

Rules a. and c. prohibit normal transitions from the ortho to parahelium states, and hence, such a transition must arise from collision (thermal) excitation. This fact creates a metastable condition at the ^3S level which is dependent on thermal excitation to decay to the ^1S ground state.

The portion of the helium spectrum which is pertinent to the magnetometer application is centered about this metastable ^3S state which is uniquely characterized by permissible photon excitation to higher energy levels and thermal relaxation to the ground state. In diagrammatic form:

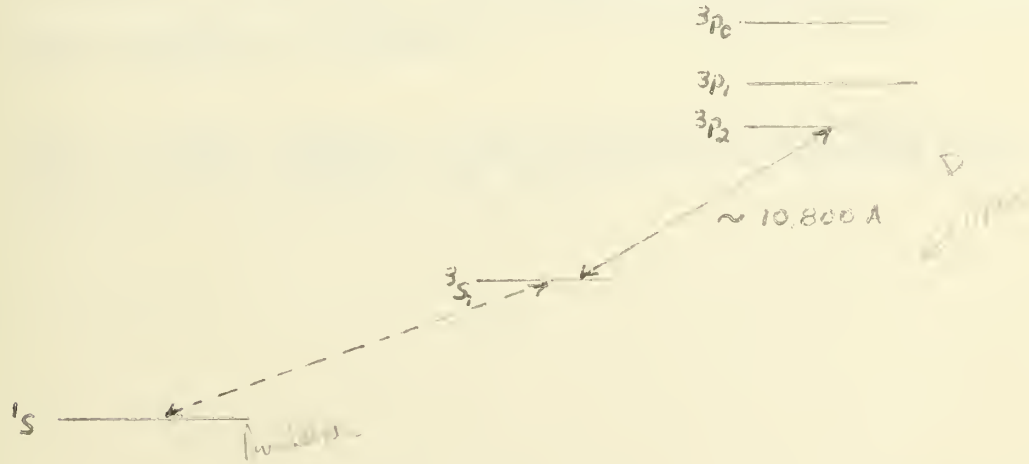

Fig. 4. Helium Spectrum in the Absence of Magnetic Field

2. The Zeeman Splitting

The rotation of the electric charges within the atom leads to the production of a magnetic moment which is proportional to the angular momentum. The effect of the magnetic moment is to cause a precessional motion when the atom is immersed in a magnetic field, and in accordance with quantum mechanics, only discrete directions in relation to the field are allowed. This means that a "space quantization" of the total angular momentum, J, exists in a magnetic field environment, and that the total angular momentum in the direction of the field will take on only discrete values. It can be shown[6] that there are 2J+1 such values, hence, there are 2J+1 energy sublevels for each field-free state. The actual energy associated with each sublevel depends on the product of the magnetic field intensity and the component of the magnetic moment in the field direction.

In the case of orthohelium, the so-called anomalous Zeeman splitting is observed. Because of the Lande g-factor involved with this effect, the mathematical consideration of the Zeeman energy is developed in Appendix A. In diagrammatic form the Zeeman splitting can be shown as in Figure 5.

[6]N. F. Mott, Elements of Wave Mechanics, Cambridge Press, 1952, pp. 79, Herzberg, (4) pp 106.

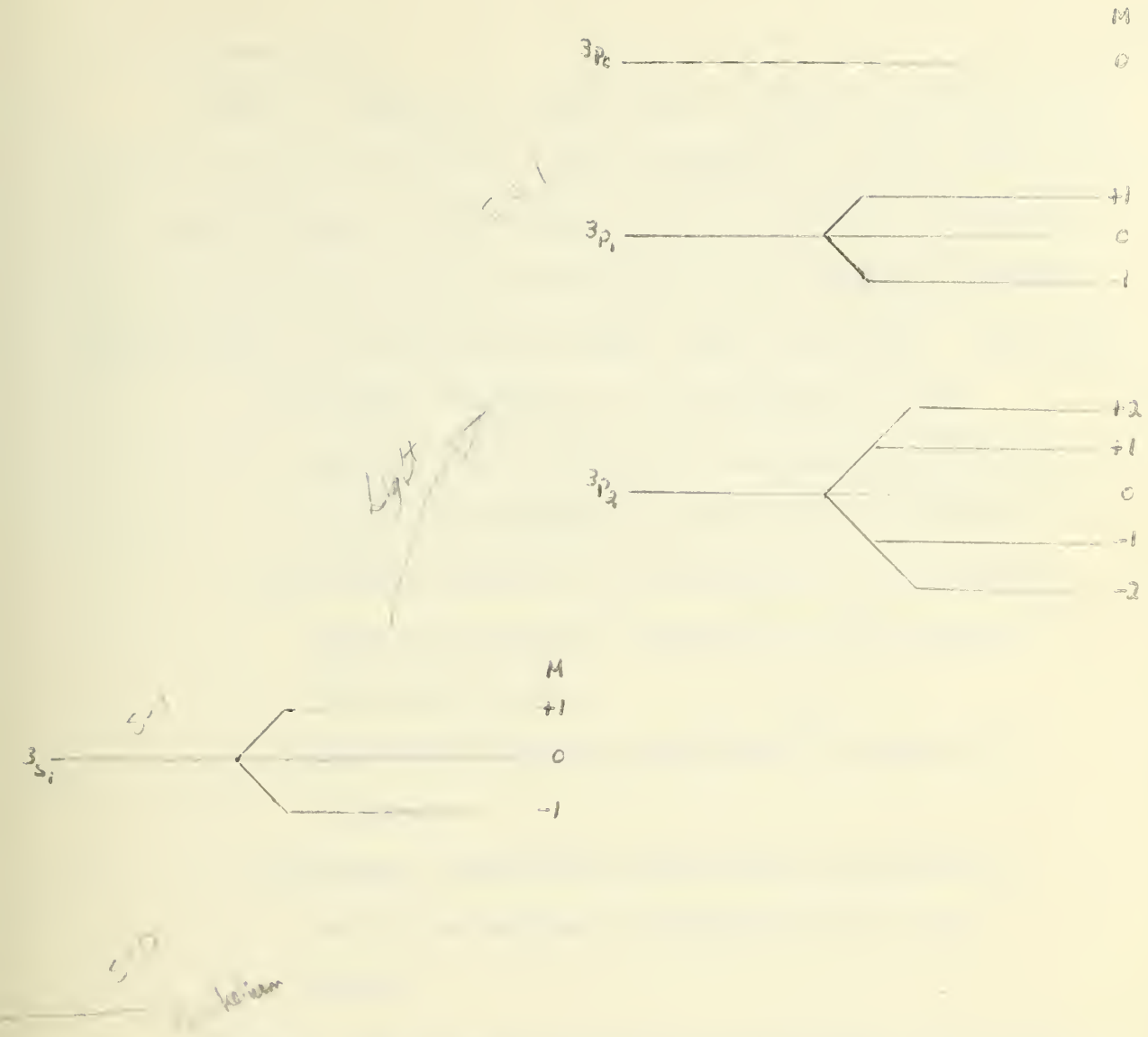

Fig. 5. Helium Energy Levels Showing Zeeman Splitting

3. The Transitions

As shown in Appendix C, there are 18 allowed transitions between the ^3S and ^3P states. The wavelengths of these lines are in the near infra-red. (1.08 microns) In the presence of external photon excitation, there are essentially four separate actions which effect the transitions between these two states. These are:

(a) Induced absorption in the presence of the pumping light which cause a transition from one of the ^3S sublevels to one of the ^3P sublevels.

(b) Induced emission in the presence of the pumping light which cause a transition in the opposite direction to (a).

(c) Spontaneous emission from the ^3P levels to the ^3S levels.

(d) Thermal relaxation effects which effectively retire and replace metastable atoms in all levels.

Of these, the second is generally considered to have little influence on the problem due to the short lifetime of the atom in the ^3P state. ($\sim 10^{-8}$ sec.) Each of the remaining effects have a finite individual probability of occurrence for each level, although the thermal effects are usually considered equally probable for all ^3S sublevels. The lifetimes of the metastable atoms have been measured and fall in the range of 10^{-4} to 20×10^{-3} sec.

As shown in Appendix B, the effect of using a circular polarizer is to limit the allowed transitions to a total of six, which are those involving a ΔM of plus or minus one depending on the direction of polarization. This in turn radically changes the sublevel population densities as shown in Appendix C, and as a further result, a net magnetic moment is formed. It is this net atomic magnetic moment that will allow analysis of the system ensemble on the basis of a magnetization vector per unit volume which will follow under the consideration of signal development.

4. The Larmor Precession Process

In Appendix A the Zeeman sublevel difference is considered from the viewpoint of an energy relation. It is of equal importance to consider the precessional effects associated with this energy, for each is related to the other by the familiar relation:

$$\Delta E = h f \tag{1}$$

From Appendix A, equation (10):

$$\mu_J = -\mu_B g \sqrt{J(J+1)}$$

where μ_J - atomic magnetic moment

μ_B - Bohr magneton

g - Lande g-factor

$\sqrt{J(J+1)}$ - net atomic angular mementum in units of $\frac{h}{2\pi}$

For convenience let $\bar{S} = \bar{a}_J \sqrt{J(J+1)}$ be called the "spin" vector.

Then: $\bar{\mu}_J = -\mu_B g \bar{S}$

But: $\frac{\mu_J}{\frac{h}{2\pi}\sqrt{J(J+1)}} = \frac{eg}{2mc} = \gamma$, the gyromagnetic ratio.

Hence:

$$\bar{\mu} = -\gamma \hbar \bar{S} \qquad \hbar = \frac{h}{2\pi}$$

And since:

$$\text{Torque} = \bar{\mu} \times \bar{H}$$

$$\bar{T} = -\gamma \hbar (\bar{S} \times \bar{H})$$

But, torque = $\frac{d}{dt}$ (angular momentum)

so: $\bar{T} = \frac{d}{dt}(\hbar \bar{S})$

and: $\frac{d\bar{S}}{dt} = -\gamma(\bar{S} \times \bar{H})$

which can be written as a scaler:

$$\frac{dS}{dt} = \gamma S H \sin\theta$$

Let the spin S rotate around H an increment ΔS corresponding to an angle $\Delta\beta$. Then:

$$\Delta\beta = \frac{\Delta S}{S \sin\theta}$$

and:

$$\omega = \text{angular velocity} = \frac{d\beta}{dt} = \frac{\gamma S H \sin\theta}{S \sin\theta} = \gamma H$$

Hence, for a magnetic moment of μ_J, there is a precession around the H field at an angular rate ω. If the field is H_o then there is a unique rate, ω_o associated with the precession.

But, note that this frequency corresponds to the energy of the precession as developed in Appendix A, where $\Delta M = 1$. Equation (12) there, was:

$$\Delta E = g \mu_B H(\Delta M)$$

For the ^3S levels, a short calculation will reveal g = 2, and from (1): $\frac{f}{H} = \frac{2\mu_B}{h}(\Delta M) = \frac{2\mu_B}{h}$

$$\frac{f}{H} = \frac{2(0.92712 \times 10^{-20})}{6.623773 \times 10^{-27}} = 2.8 \text{ mc/gauss} = 28 \text{ cps/gamma}$$

where 1 gamma = 10^{-5} gauss.

Since the earth's field is nominally one-half gauss, the resonant frequency used in the helium magnetometer is 1.4 mc.

B. The Signal Development

1. The Pumping Process

It is of interest to consider a rotating frame of reference. Let it be assumed that the spin vector is standing still in a fixed frame of reference, and the observer is rotating at angular rate ω. To the observer the spin vector will appear to be rotating backwards, and it will move through the angle $\Delta\beta$ in the time Δt. From Figure 6, it can be seen that $\Delta S = \Delta\beta S \sin\theta$ so $\frac{\Delta S}{\Delta t} = \omega S \sin\theta$ or $\left(\frac{d\bar{S}}{dt}\right)_{rot} = \bar{S} \times \bar{\omega}$. But, it is possible that $\bar{S}$ could be moving with respect to the fixed frame so the total movement is given by:

$$\left(\frac{d\bar{S}}{dt}\right)_{rot} = \bar{S} \times \bar{\omega} + \frac{d\bar{S}}{dt}$$

If there exists a magnetic field in the direction of the Z axis, the Larmor precession is: $\frac{d\bar{S}}{dt} = -\gamma(\bar{S} \times \bar{H})$

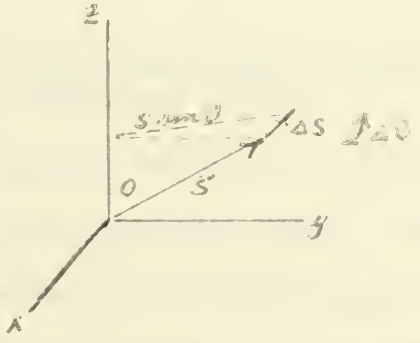

Fig. 6. Fixed Reference Frame

Hence, the total apparent rotation is:

$$\left(\frac{d\bar{S}}{dt}\right)_{rot} = \gamma\bar{S} \times \left(\frac{\bar{\omega}}{\gamma} - \bar{H}\right)$$

But, note from the equations concerning the Larmor precession that this is equivalent to a magnetic field in the rotating frame which has the value: $\bar{H}_{eff} = \bar{H} - \frac{\bar{\omega}}{\gamma}$

Now consider a pumping light modulated by a square wave at the Larmor frequency, which is oriented along the X axis of a fixed frame. For simplicity, let it be assumed that the light is "on" only when the X axis of the fixed frame is aligned with the X' axis of the rotating frame:

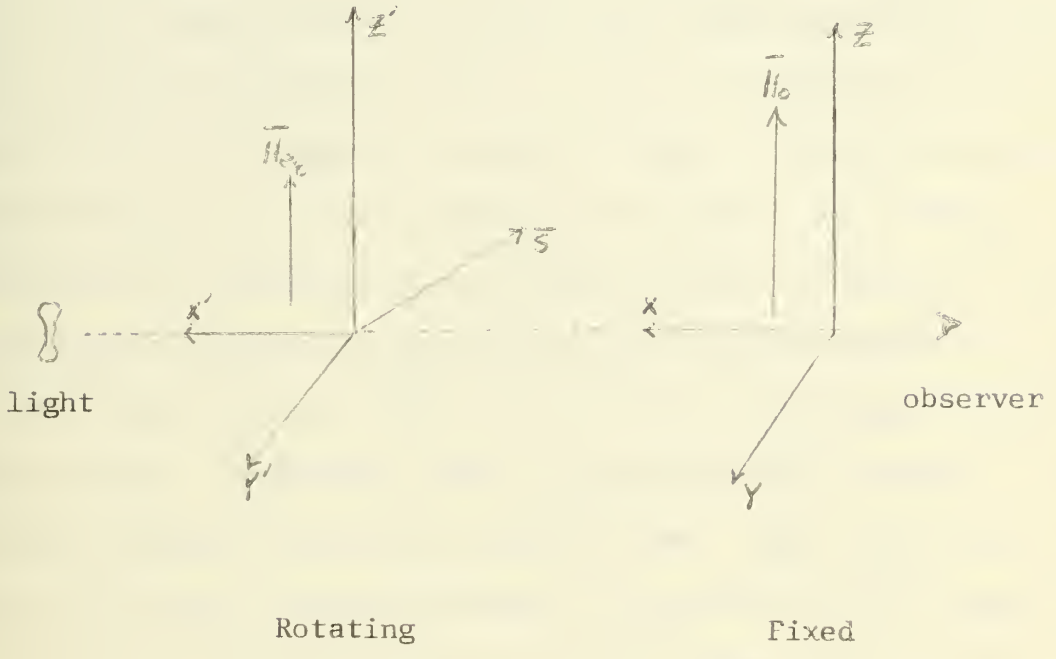

Fig. 7. The Precessional Reference Frames with Modulated Light.

If the angular velocity is such that $\frac{\omega_c}{\gamma} = H_c$ there is no residual field in the rotating frame. Further, the conditions are the same if the observer were standing <u>on</u> the rotating frame in a darkened room with the pumping light blinking in synchronization with the rotation. The observer sees no magnetic field and no movement of the spin vector in the rotating frame of reference. This situation describes a static condition of no torque, and hence, there is a minimum of light absorption which might be ascribed to the magnetic field effects.[7]

[7]cf, J.R. Singer, (5), pg. 48

A closer examination of this resonant condition will reveal a space quantization along the X' axis which is due to the pumping light alone. This effect, first suggested by Kastler[8], was later established experimentally by Hawkins (7) using sodium atoms. In effect, the space quantization is the same as the magnetic effects previously described, i.e., there exists preferred orientations of spin vector in relation to the X' axis in the presence of the pumping light and in the absence of magnetic field. It has been shown in Appendices A and B that transitions involving a unit change in angular momentum are associated with polarized light. If the spin vector position was defined to be positive when pointed towards the observer, an absorption process would occur when the vector points towards the light source. Conversely, when the vector points towards the observer, minimum energy is extracted from the beam. Under these conditions, the spin vector is pointed towards the observer at all times when resonance is established in the rotating frame. This is the equilibrium "pumped" condition of the sample, and no transitions are occurring if relaxation effects are ignored.

The "off-resonance" conditions immediately establish a residual magnetic field, H_{eg} oriented parallel to the Z' axis which has a magnitude $H_o - \frac{\omega}{\gamma}$. The spin vector precesses about this residual field, bringing it into position to be "pumped" back to its equilibrium position. Absorption caused by the pumping process is due to partial mixing among the Zeeman sublevels, and if H_{eg} becomes very large, complete mixing will occur.

[8]A. Kastler, Proc. Phys. Soc. A67, 853 (1954).

It can be assumed that the spin vector motion during this "off-resonance" condition will transcribe a complex pattern in space. However, a simplified picture can be obtained by averaging random instantaneous "snapshots" of the process by displaying them in a continuum. The result in the vicinity of resonance might show an "expectation cone" as the surface of movement, which is oriented towards the observer:

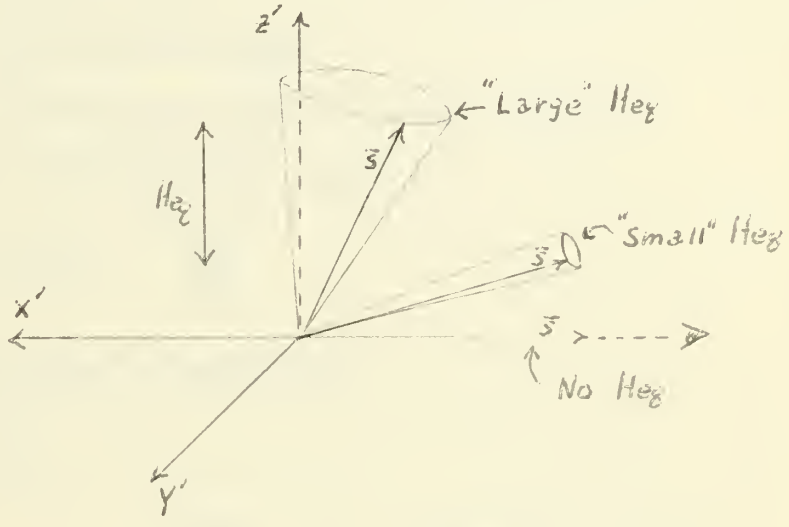

Fig. 8. Expectation Position of the Spin Vector in a Rotating Frame

It can be noted that the net effect is not unlike the now-standard resonance conditions using an externally applied RF field at right angles to the static field.

2. The Phenomological Approach

Since a net magnetic moment exists, it is convenient to consider a more quantitative viewpoint of the resonance phenomena. To do this, the individual atomic vector parameters may be combined to give:

$\bar{M}$ - The net instantaneous resultant magnetic moment per unit volume which is parallel to the angular momentum vector.

$\bar{A}$ - The instantaneous resultant angular momentum per unit volume.

$\bar{T}$ - The total torque.

$\bar{H}$ - The static magnetic field intensity.

The classical relation between these is:

$$\bar{T} = \bar{M} \times \bar{H} = \frac{d\bar{A}}{dt}$$

On the atomic scale, by definition:

$$\bar{\mu} = \gamma \bar{a}$$

where: γ - gyromagnetic ratio

$\bar{\mu}$ - atomic magnetic moment

$\bar{a}$ - atomic angular momentum

Hence, by analogy:

$$\bar{M} = \gamma \bar{A}$$

Combining the above relations gives a result which is similar to the previously considered precession equations:

$$\frac{d\bar{M}}{dt} = \gamma [\bar{M} \times \bar{H}] \qquad (1)$$

Let the magnetic field be parallel to the Z axis. The major portion of the precession energy is due to the magnetic field and can be written:

$$E = -H_0 M_z$$

Energy changes due to thermal perturbations will be then caused by changes in M_z . Let M_c represent the equilibrium value of M_z . If $M_z \neq M_c$, it will approach this value exponentially with a time constant T_1 , which is the "thermal" or "longitudinal" relaxation time. Therefore:

$$\frac{dM_z}{dt} = \frac{-(M_z - M_c)}{T_1} \qquad (2)$$

Processes which do not effect the total energy can be attributed to an "effective irregularity" in the magnetic field of order H' These effects can be characterized by a "transversal relaxation time":

$$T_2 = \frac{1}{\gamma H'}$$

Assuming that the transverse effects are essentially exponential in character:

$$\frac{dM_x}{dt} = -\frac{M_x}{T_2} \qquad \frac{dM_y}{dt} = -\frac{M_y}{T_2} \qquad (3)$$

and that these effects can be summed:

$$\frac{dM_x}{dt} - \gamma\left[\bar{M}\times\bar{H}\right]_x + \frac{M_x}{T_2} = 0$$

$$\frac{dM_y}{dt} - \gamma\left[M\times H\right]_y + \frac{M_y}{T_2} = 0$$

$$\frac{dM_z}{dt} - \gamma\left[\bar{M}\times\bar{H}\right]_z + \frac{M_z}{T_1} = \frac{M_0}{T_1}$$

These equations define the motion of the macroscopic magnetic moment with the magnetic field in the Z direction.

3. The Optical Modulation

The previous phenomological equations were developed under the simplifying conditions that the equilibrium position coincided with the magnetic field. However, from the intuitive approach presented previously, it is obvious that the equilibrium position for the present case is in the direction of the X axis for observation along the X axis. The relaxation factors then will take the form:

$$\frac{dM_x}{dt} = \frac{M_0 - M_x}{T_2} \qquad \frac{dM_y}{dt} = -\frac{M_y}{T_2} \qquad \frac{dM_z}{dt} = -\frac{M_z}{T_1}$$

It is also necessary to modify the equations for the effect of the pumping light. Consider, for example, the effect of an unpumped sample being irradiated with the pumping light. The rate of change of one sublevel could be expressed in terms of the number of atoms remaining in that level and the pumping rate. In a similar manner, the rate of change of the X component of the net magnetic moment can be expressed as the difference between the final magnitude and the instantaneous magnitude times the pumping rate:

$$\left(\frac{dM_x}{dt}\right)_{PUMP} = (M_0 - M_x)P_x \qquad \left(\frac{dM_y}{dt}\right)_{PUMP} = -M_y P_x \qquad \left(\frac{dM_z}{dt}\right)_{PUMP} = -M_z P_x$$

Combining these relations with (1) of the previous section:

$$\frac{dM_x}{dt} - \gamma\left[\bar{M} \times \bar{H}\right]_x + \frac{M_x}{S_{c2}} = \frac{M_0}{S_2} \qquad (1)$$

and similarly for the other two equations:

$$\frac{dM_y}{dt} - \gamma[\bar{M} \times \bar{H}]_y + \frac{M_y}{S_2} = 0 \qquad (2)$$

$$\frac{dM_z}{dt} - \gamma[\bar{M} \times \bar{H}]_z + \frac{M_z}{S_1} = 0 \qquad (3)$$

where: $S_1 = \frac{1}{P_x + \frac{1}{T_1}}$ $S_2 = \frac{1}{P_x + \frac{1}{T_2}}$ P_x = Pumping rate

These are the equations of motion of the net magnetic moment for a pumping light oriented at right angles to the magnetic field and are attributed to Bell and Bloom (9).

Since the precession will be around the magnetic field, the net XY magnetic moment will be rotating circularly in time. It is of interest to consider this time relation, so let:

$$F = M_x + i M_y \qquad (4)$$

Inserting $\bar{H} = H_o \bar{a}_z$ and combining (1) through (4):

$$\frac{dF}{dt} + i\gamma H_o F + \frac{F}{S_2} = \frac{M_o}{S_2} \qquad (5)$$

$$\frac{dM_z}{dt} + \frac{M_z}{S_1} = 0 \qquad (6)$$

Due to the light modulation, M_c will be a function of time; so the solution of (5) must be restricted by defining:

$\mathcal{M}_c$ – The polarization that would be produced in the absence of magnetic field and thermal relaxation effects, such that:

$$M_c = \mathcal{M}_c P_\lambda S_z$$

Equation (5) is then:

$$\frac{dF}{dt} + i\gamma H_0 F + \frac{F}{S_z} = \mathcal{M}_c P_\lambda \tag{7}$$

Now let the light be modulated by defining:

$$P_\lambda = a + b \cos \omega t$$

$$\frac{1}{S_z} = R + b \cos \omega t$$

Looking for solutions of the form:

$$F = f_1 e^{i\omega t} + f_{-1} e^{-i\omega t}$$

and separating like components of interest:

$$f_1 \left[i\omega + i\gamma H_0 + R \right] = \frac{b \mathcal{M}_c}{2}$$

$$f_{-1} \left[-i\omega + i\gamma H_0 + R \right] = \frac{b \mathcal{M}_c}{2}$$

The only terms which give an observable magnitude are those associated with f_{-1} since at resonance:

$$\omega_0 = \gamma H_0$$

Hence:

$$f_{-1} = \frac{b \mathcal{M}_c}{2} \left[\frac{R - i(a\omega)}{R^2 + (a\omega)^2} \right] \qquad \omega_0 = \gamma H_0 - \omega$$

where: $\Delta\omega = \gamma H_0 - \omega$

From the previous discussion of the pumping process, it can be concluded that the light absorbed would be proportional to $P_x(1-M_x)$, so taking the real part of F :

$$P_x(1-M_x) = a + b\cos\omega t - \frac{ab\,m_0 R}{2}\frac{\cos\omega t}{R^2+(\Delta\omega)^2} - \frac{b^2 m_0 R}{2}\frac{\cos^2\omega t}{R^2+(\Delta\omega)^2}$$

Using a sweep field frequency which is slow compared to the precession frequency and a detector insensitive to the precession frequency will result in a signal proportional to:

$$\frac{R b^2 m_0}{4\left[R^2+(\Delta\omega)^2\right]}$$

For a light direction vector lying at the angle θ from the pole axis (magnetic field), the P_x and M_x above will contain a $\sin\theta$ dependence resulting in the signal strength correction $\sin^2\theta$. In addition, if the light modulation index is designated m, the signal will take the form:

$$S_x \propto \frac{R m^2 a^2 m_0 \sin^2\theta}{4\left[R^2+(\Delta\omega)^2\right]}$$

It can be seen that the signal will increase with the square of the modulation index; the light intensity and/or the sine of the angle between the magnetic field and the light directions.

4. The Line Shape

For a given set of operating conditions, the signal equation can be written:

$$S = \frac{K}{1 + \zeta^2} \qquad \zeta = \frac{\Delta\omega}{R}$$

If the frequency is varied through the line center ($\gamma H_0 = \omega_0$), the one-half amplitude line width is defined by:

$$\frac{\gamma H_0 - \omega_{1,2}}{R} = \pm 1$$

and therefore, the line width is:

$$\omega_1 - \omega_2 = \Delta\omega_\ell = 2R$$

From the original definition of R :

$$R = a + \frac{1}{T_2}$$

$$= \frac{1}{T_p} + \frac{1}{T_2}$$

where: a - The average pumping rate

T_2 - The metastable relaxation time

T_p - Average pumping time

the line width would be:

$$\Delta\omega_\ell = 2\left(\frac{1}{T_p} + \frac{1}{T_2}\right)$$

These times are difficult to predict for a given working situation. Colgrove and Franken (2) have measured T_2 and found it to be about one quarter of a millisecond for a fixed condition of pumping light intensity, absorption cell size and pressure. In addition, this time was measured using unpolarized light. Phelps and Molnar[9] have investigated the metastable lifetime in some detail and have measured lifetimes as high as 20 milliseconds. From this work, a reasonable estimate for the present case might be in the order of 10^{-4} seconds when the cell pressure is 0.5 mm Hg. If it can be assumed that T_1 is of the same order of magnitude, the approximate line width would be:

$$\Delta\nu \cong \frac{2}{\pi} \times 10^4 \text{ cps}$$

$$\cong 6400 \text{ cps}$$

[9] A.V. Phelps and J. P. Molnar, Lifetimes of Metastable States of Noble Gases, Phys. Rev. 89, 1202, (1953).

III. The Theoretical Magnetometer System

A. General Design

Instead of sweeping the resonance oscillator to obtain a signal as in previous examples, it is usually more convenient to modulate the magnetic field at a slow (audio) rate. The comparison of the resulting signal with the sweep field cycle then allows a simple loop control:

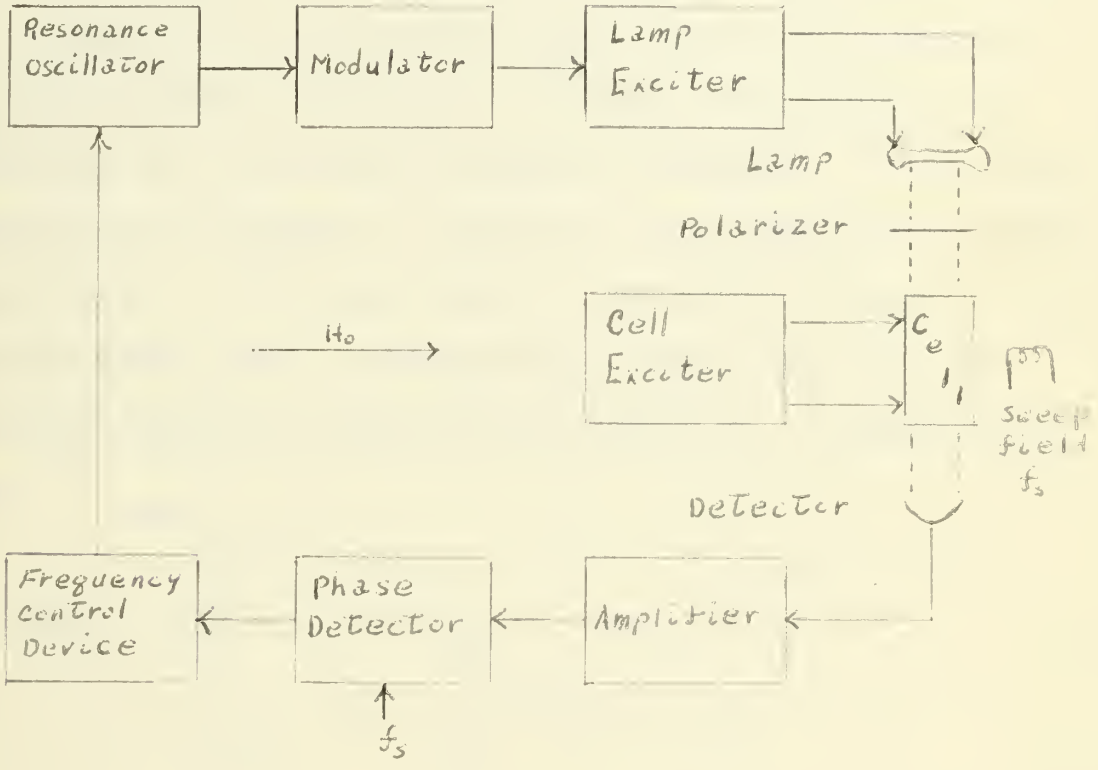

Fig. 9. The Theoretical Magnetometer System

To obtain a bright pumping light source, the lamp is driven by a high frequency exciter which is modulated in some manner at the resonance frequency. The exact exciter frequency is not critical to the operation, provided it can be modulated at 1.4 mcs.

The absorption cell is also provided with a radio frequency source to cause ionization with subsequent production of metastable atoms. Again, the exact frequency is a matter of convenience, but less power is required at higher frequencies.

The photodetector can be any type sensitive to the near infrared spectrum which can respond to a frequency twice that of the sweep field. The lead sulphide detector is well suited to this application if the sweep frequency is selected below about 1000 cps.

In operation, the change in light intensity associated with the ambient magnetic field causes a change in the photodetector output each time the sweep field passes through zero. This signal is amplified and compared to the phase of the sweep field to detect a system error. If an error exists, a corrective voltage is developed which causes a corresponding change in the resonance oscillator frequency to match the new condition. In diagrammatic form:

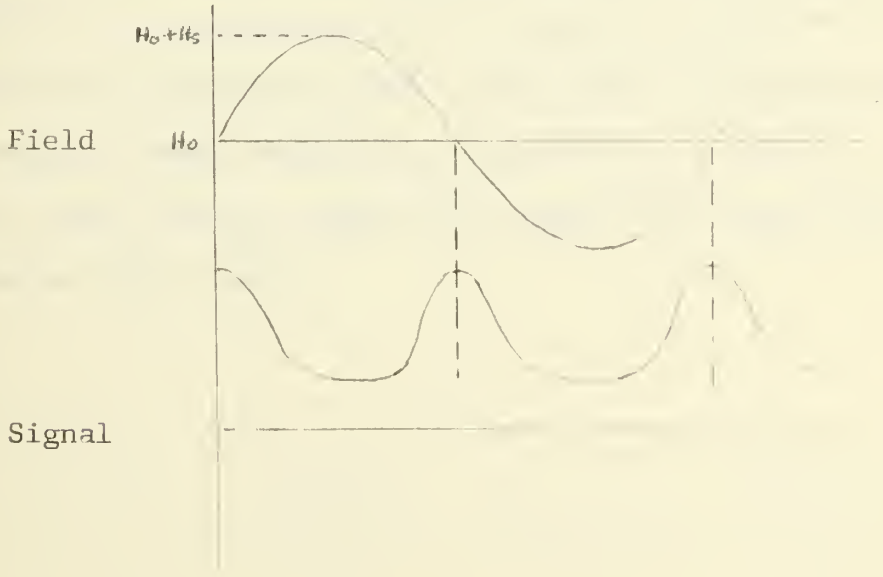

Fig. 10. Phase Detector Operation when $\omega = \gamma H_o$

When the instantaneous frequency does not match the ambient field, the signal peaks will be shifted to give a resultant direct current output:

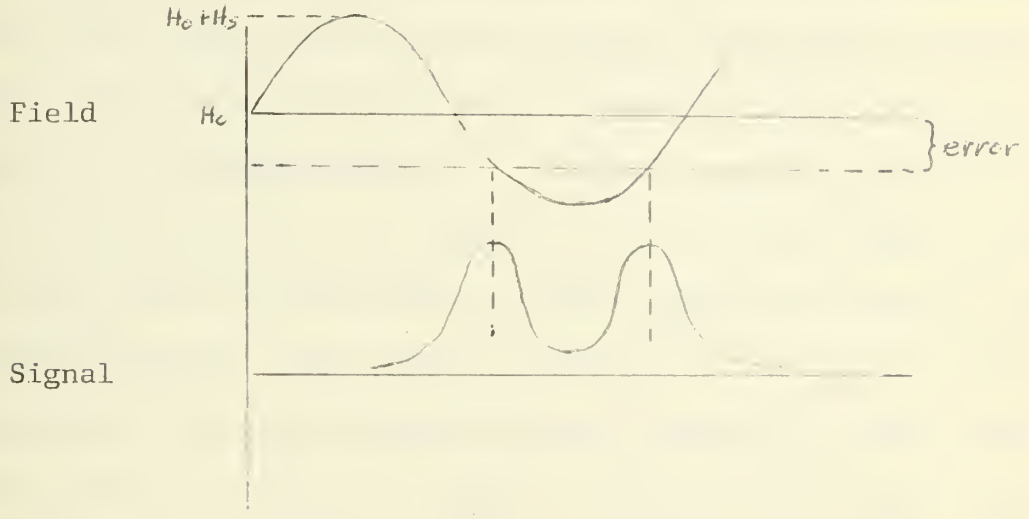

Fig. 11. Phase Detector Operation when $\omega \neq \gamma H_o$

This is an over-simplified representation of the actual operation, since it is assumed that the signal is inserted into the phase detector as a polarized pulse. For narrow line width compared to the magnetic sweep magnitude, $\Delta\omega_\ell << \gamma H_s$, this is not a serious error, since then the signal will appear as a short pulse on an otherwise linear sweep.

B. The Consideration of Noise

Since the phase detector is the loop error control device, it is instructive to examine its operation in some detail.

The processing of the raw signal could conceivably take many forms from linear amplification to actual construction of a new signal from some correlation device inserted between the photodetector and the phase detector. However, the phase detector operation is generally quite indifferent to the average shape of the operating signal, and the experimental system complexity should be kept to a minimum consistant with adequate performance. In light of these considerations, the signal processing must consist of simple amplification with, perhaps, limiting to remove variations in the signal amplitude. The following assumptions form a model quite similar to the experimental conditions:

a. The signal is limited to such an extent that a polarized trapezoidal pattern results.

b. The trapezoidal sides have the same slope as the original signal at the one-half amplitude point.

c. An "ideal" phase detector is used which has the following form:

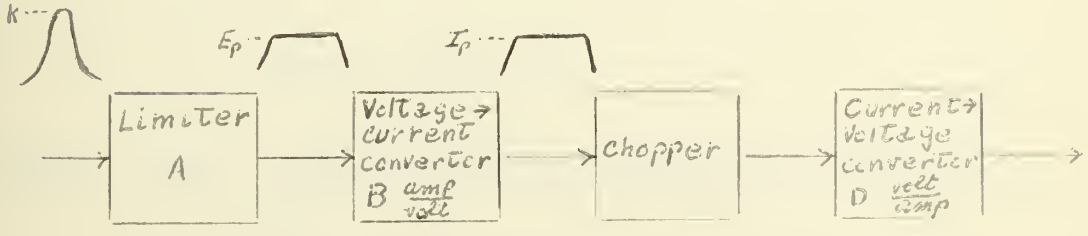

Fig. 12. Signal Processing Chain

Let the chopper transient occur at the zero crossover of the sweep field cycle as follows:

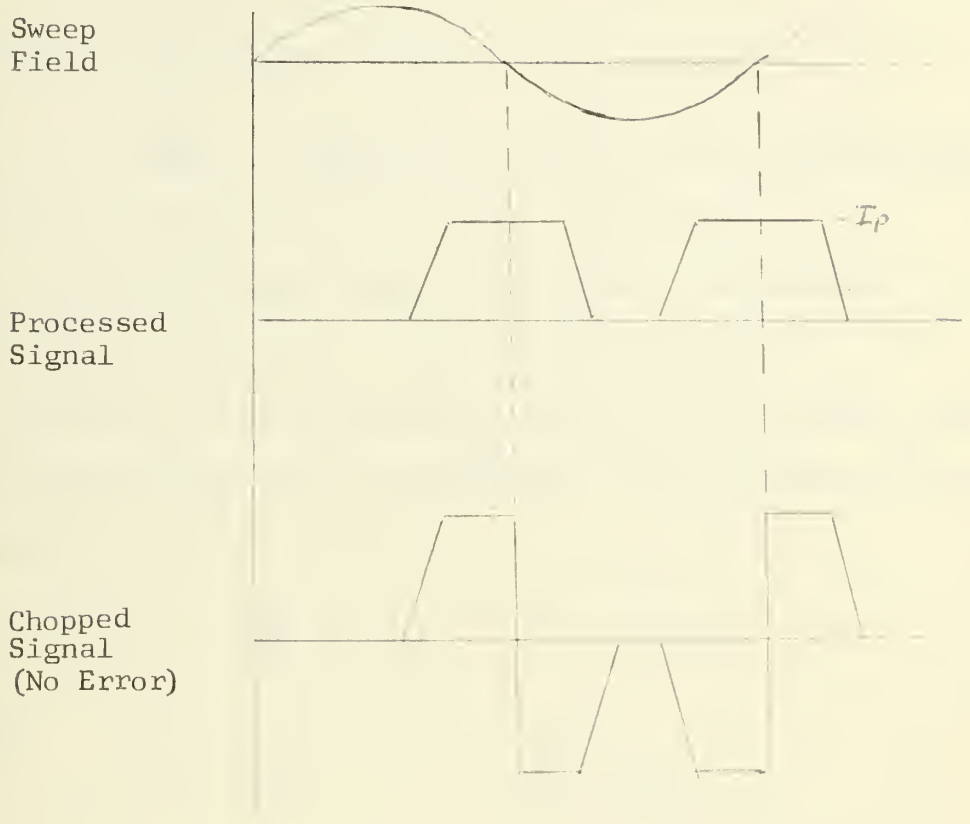

Fig. 13. Phase Detector Waveforms

If the current-to-voltage convertor is a capacitor and the signal error is small compared to the trapezoidal width:

$$\Delta E_e = \frac{4 I_p}{C} \Delta T_e \qquad (1)$$

where: ΔE_e is the error voltage output per sweep field cycle.

ΔT_e is the time displacement of the processed signal from the mean.

Due to the severe limiting of the signal, the input noise fluctuations will only result in a displacement of the trapezoid:

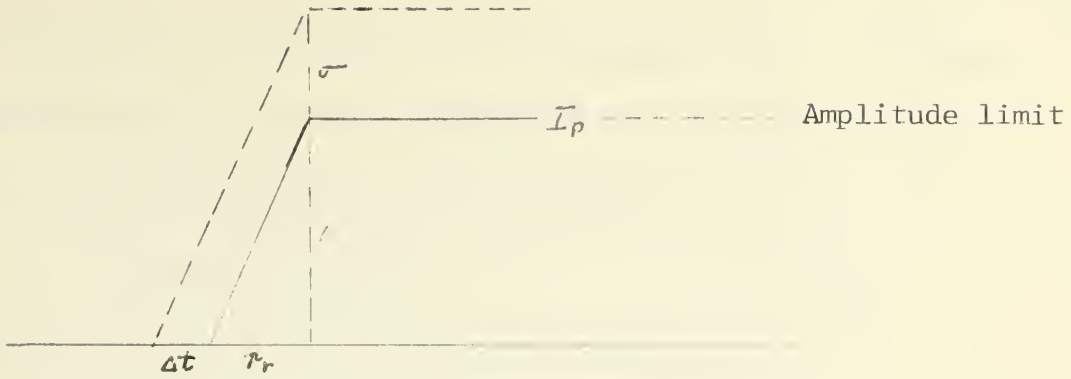

Fig. 14. Noise Variations in the Processed Signal

where: σ is the rms value of the input noise

Δt is the rms value of the noise displacement

τ_r is the time of rise of the trapezoid

The slope of the unprocessed signal at the one-half amplitude point can be found by differentiation of the signal equation and substitution of the relation:

$$\zeta = \frac{\zeta H_0 - \omega}{R} = 1$$

Hence:

$$S = \frac{K}{1+\zeta^2} = \frac{K'}{R^2 + (\zeta H_0 - \omega)^2}$$

$$\frac{dS}{d\omega} = \frac{2KR^2(\zeta H_0 - \omega)}{R^4\left[1 + \left(\frac{\zeta H_0 - \omega}{R}\right)^2\right]^2}$$

$$\left.\frac{dS}{d\omega}\right|_{1/2} = \frac{K}{2R}$$

But the one-half amplitude line width was previously determined to be $2R$, so

$$\text{slope}_{\frac{1}{2}} = \frac{K}{\Delta\omega_l}$$

The field is being swept at a low audio rate. If this corresponds to a resonance frequency rate of W_h radians/sec^2, the slope of the signal in time will be:

$$\text{slope} = \frac{K}{\Delta \omega_l} W_h$$

and the relation with the processed signal is:

$$\frac{ABK}{T_r} = \frac{BKW_h}{\Delta \omega_l}$$

where the dimension change BK amperes is necessary to maintain a constant amplitude ratio and like units. From the similar triangle relations of the trapezoid:

$$\frac{\Delta t}{B\sigma} = \frac{T_r}{I_p} = \frac{\Delta \omega_l}{BKW_h}$$

The rms uncertainty in signal position due to noise is therefore:

$$\Delta t = \frac{\sigma(\Delta \omega_l)}{K W_h}$$

From (1):

$$\Delta E_e = \frac{4ABK}{C W_h} \left(\frac{\Delta \omega_l}{K/\sigma} \right)$$

And the "rms error voltage per unit signal per cycle" is:

$$\frac{\Delta E_e}{K} = K'' \left(\frac{\Delta \omega_l}{K/\sigma} \right)$$

Although further processing will modify the actual error due to noise, the line width/signal-to-noise relation will determine the input error. The conclusion is: The magnitude of the noise error is proportional to the line width and inversely proportional to the signal-to-noise ratio.

IV. The Experimental Magnetometer System

A. Principles of Construction

The guiding principles for construction of the magnetometer were:

1) Obtain a low line width/signal-to-noise ratio consistant with local conditions.
2) Use standard equipment where possible.
3) Provide variable filtering and system gains to optimize the field tracking ability.

To optimize the line width/ signal-to-noise ratio there must be homogeneity of the magnetic field within the absorption cell and an orientation of the optical system perpendicular to the local field. The magnetic field direction near the system location was found to be 33 degrees from the vertical. Previous experiments had indicated that a maximum signal-to-noise ratio of approximately ten could be achieved in the vertical position, and the optical system was so mounted, although this represented a theoretical signal amplitude which was 30% of that obtainable in the optimum orientation. This decision considerably eased the optical-structure details. The field homogeneity was dictated by local working space, the equipment location and orientation, and the total field-shaping efforts. Efforts were made to use non-magnetic components in the immediate vicinity of the cell (a few feet), but beyond this no particular efforts were made to improve the gross field.

B. The System Description

Following the general design of the theoretical magnetometer, the experimental equipment was assembled into the form shown in the following block diagram:

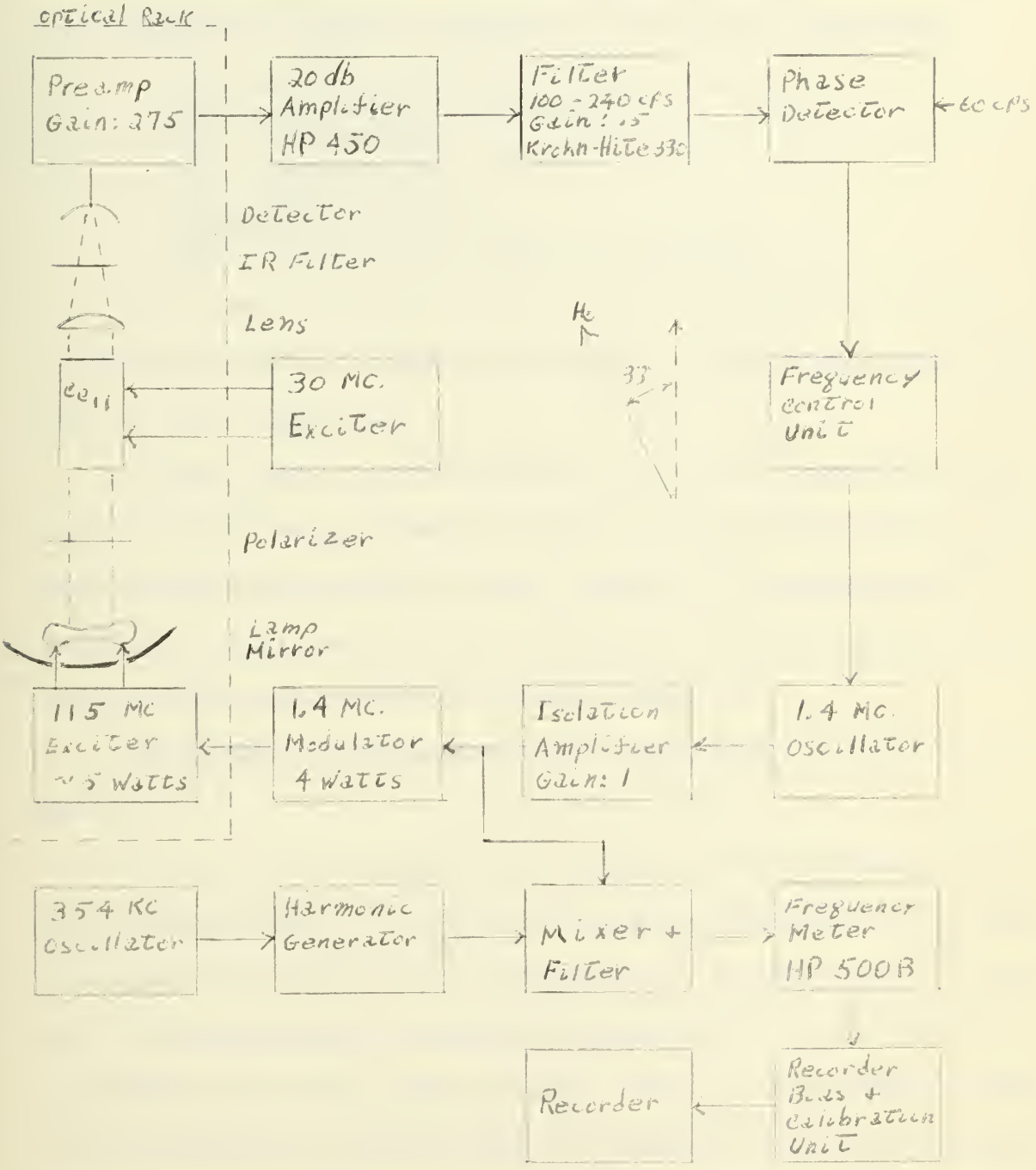

Fig. 15. The Experimental Magnetometer System

Due to the high stray 60 cps magnetic fields found in the area, no additional sweep field was used. The magnitude and phase of this field could be adjusted slightly by proper orientation of major components using 60 cps power-primarily power supplies.

The major commercial equipments used in the system were:

V.A. 354 kc. Oscillator
V.A. Mixer and 0-3 kc Filter
V.A. G-10 Recorder
H.P. Frequency Meter 500B
H.P. Amplifier 450A
Krohn-Hite Filter 330A
Kodak Ektron Photoconductive Detector

The schematic drawings of the remaining equipments are included in Appendix D, with the exception of the 30 mc exciter and the isolation amplifier.

Filament power for the modulator, the 115 mc exciter and the 30 mc. exciter was provided by battery, and the high voltage supply was provided from commercial power supplies. The preamplifier, frequency control unit, 1.4 mc. oscillator, harmonic generator and recorder bias were completely battery supplied.

Photographs of the working system are shown in Figs. 16, 17 and 18.

The heart of the magnetometer system is the aluminum optical rack shown attached to the wall. As can be noted from the interior photograph, the helium lamp and the 115 mc. exciter occupy the lowest tier together with a spherical mirror which increases and collimates the usable pumping light. The light then passes through a linear polarizer (Polaroid HR) and a quarter wave plate, forming circularly polarized infra-red light components before entering the

absorption cell. The absorption cell is excited into a weak discharge by a 30 mc. oscillator connected to a pair of wire rings wrapped around the cell. (It must be noted at this point that the brilliance of the cell was increased, and that of the lamp decreased from optimum in order to obtain a photograph.) The light not absorbed in the cell continues through a short focal-length lens system (not shown), an infra-red filter to reduce exterior interference and then strikes the photodetector contained in the preamplifier unit. As the stray 60 cps magnetic field changes the total field within the cell, a decrease in the light absorption occurs when $\omega_o = \gamma H_e$. This is registered as a change in resistance at the photodetector.

The remainder of the equipment processes the signal and develops a direct-current error signal which is applied to a voltage-variable capacitor to control the 1.4 mc. oscillator for frequency-locking on the line center. The system gains are shown on the block diagram.

Modulation of the lamp is accomplished by plate and screen modulation of the 115 mc. exciter. An improvement in the signal was noted when the modulation of the exciter exceeded 100%, probably indicating that the actual light modulation is less than that of the exciter.

The magnitude of the field changes can be converted directly from the oscillator frequency by application of the factor 28 cycles/ gamma. To record the frequency variations, the fourth harmonic of a commercial crystal oscillator was mixed with the

system 1.4 mc oscillator signal to form a difference frequency in the audio range. This in turn is converted to a direct-current signal which is proportional to the difference frequency and applied through a calibration network to a pen recorder.

The major components of the system are noted on the photographs, including the field-shapers which are used to modify the field homogeneity within the cell or to adjust the total field to lie within the audio range for recording purposes.

Figure 16

The Experimental Magnetometer
- Left Hand View

1. Optical Rack
2. Detector and Preamplifier
3. Absorption Cell 30 mc. Exciter
4. 1.4 mc Modulator
5. 1.4 mc. Oscillator and Frequency Control Unit.
6. Field-Shaper
7. 20 db Amplifier
8. Active Filter
9. Phase Detector
10. Harmonic Generator
11. Power Supplies

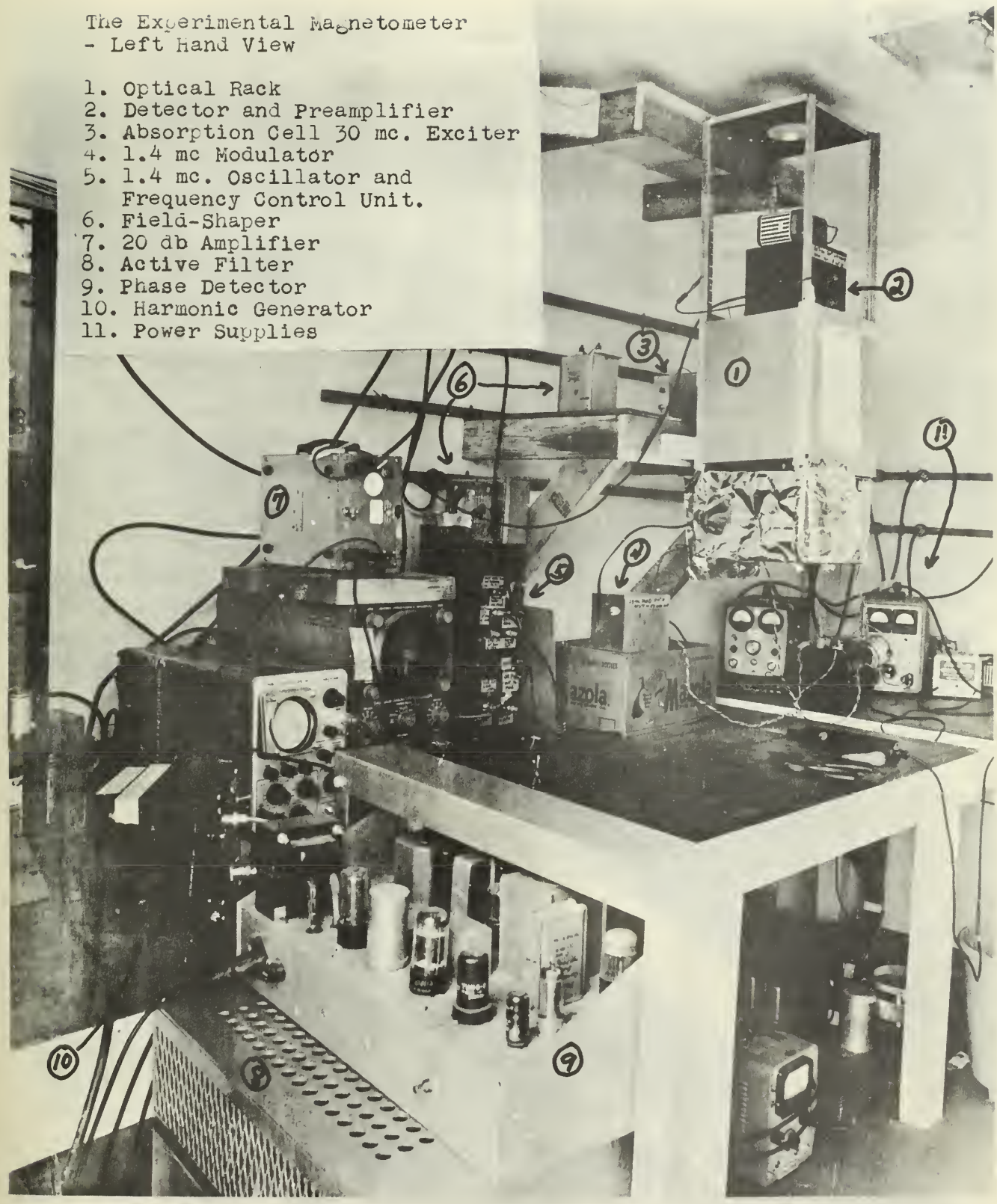

Fig. 17

The Experimental Magnetometer - Right Hand View

1. Optical Rack
2. Detector and preamplifier
3. 1.4 mc. Modulator
4. 1.4 mc. Oscillator and Frequency Control Unit
5. 20 db Amplifier
6. Active Filter
7. Phase Detector
8. 394 kc. Oscillator
9. Mixer Unit
10. Frequency Meter
11. Recorder
12. Recorder Bias and Calibrator
13. 1.4 mc. Isolation Amplifier
14. Harmonic Generator

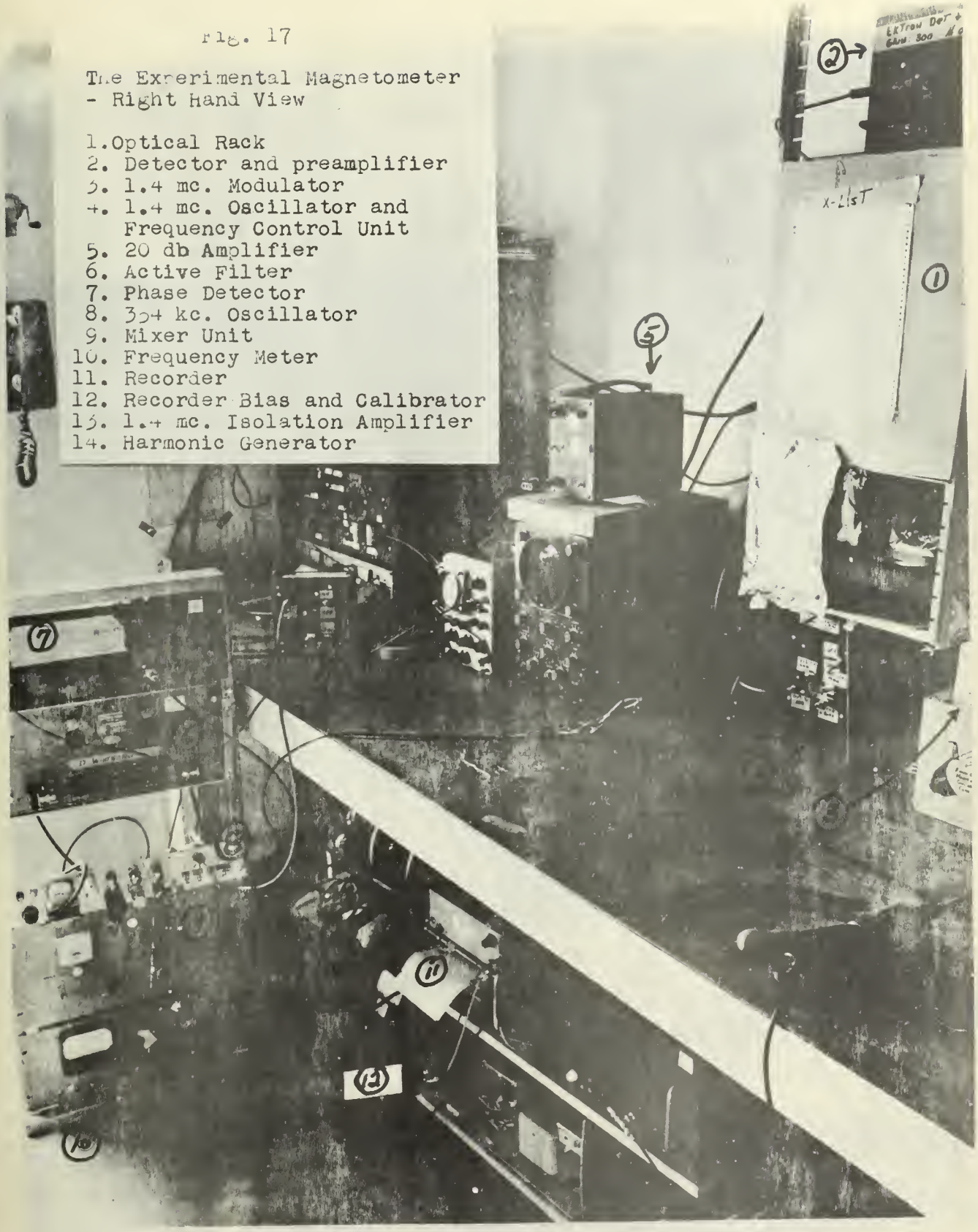

Fig. 18

The Experimental Magnetometer
- Optical Rack Details

1. 115 mc. Lamp Exciter
2. Helium Lamp
3. Spherical Mirror
4. Helium Absorption Cell

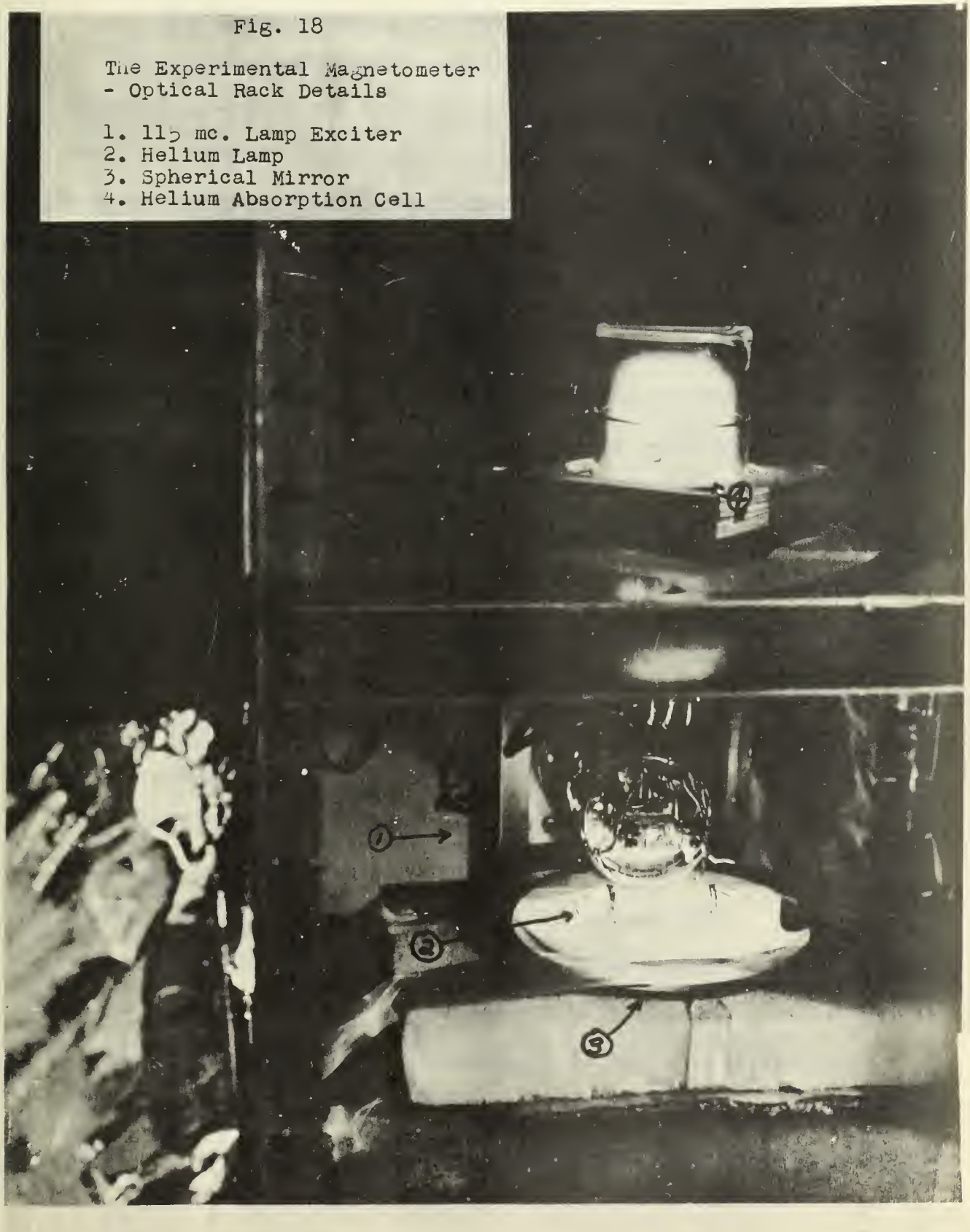

V. The Experimental System Performance

A. The Measurements of the Magnetic Field

The helium magnetometer system was designed primarily to measure changes in the magnetic field. Theoretically, the total absolute magnetic field can be obtained from the sum of the crystal frequency and the difference frequency produced by mixing the resonance oscillator and crystal frequencies. However, in the present case, only a portion of the difference frequency is used by the recorder. The portion of the difference frequency used is selected by the recorder biasing and calibration network. To further reduce noise perturbations in the recording system, a low pass filter, which has a 3 kc upper cut-off, restricts the usable difference frequency to a range 3 kc either side of the crystal frequency. Two factors, therefore, are apparent. 1) The total-field information is lost in the recording system, and only magnetic field perturbations will be recorded. 2) The magnetometer precession frequency, as taken from the resonance oscillator, must be within 3 kc of the crystal standard for recording purposes.

To record magnetic field perturbations, the magnitude of the total field within the cell was controlled by use of field-shaping metal objects which were placed near the helium system. These objects generally cause magnetic field inhomogeneity within the cell which increases the helium line width. As previously shown under the consideration of noise, an increase in the line width causes a degradation of the performance due to the contribution of noise. In the present case, this was considered acceptable in order to obtain recordings of the magnetic field.

The general performance of the experimental device was measured by simultaneous recordings with a commercial magnetometer which used rubidium as the sensing element. The rubidium sensing head was located in an open field approximately 200 feet from the helium magnetometer location.

The first closed-loop operation of the magnetometer is shown in Fig. 19. This recording, taken between 1900-2400 GMT on 27 February, 1961, shows the local mid-day diurnal change as recorded by the rubidium (left) and the helium (right). The time scale increases from bottom to top. The helium system was operating on one side of its crystal standard and the rubidium system on the opposite side of its crystal standard; so ideally, the two traces should be mirror images. Due to the experimental nature of the helium system, a certain degree of frequency drift was experienced in this recording. The broadening of the helium trace is attributed to damped oscillations of the servo-loop. The primary objective of this recording was to test the system ability to track a slow and relatively predictable change in the magnetic field. A smaller change was also recorded simultaneously by both systems (see Fig. 19).

The second recording is shown in Fig. 20. The upper trace pair is a time-continuation of the lower trace pair, and the helium system output is the upper trace. Disturbances between 1500-1530 were caused by movement of the operator within the room containing the magnetometer. The disturbance near 1730 was caused by operation of electrical equipment in a nearby building. An approximate

two gamma shift was experienced at 1720 due to changes in the magnetic sweep (60cps), so the graph was broken at this point and moved upward to match the general field movement. Signal-to-noise decrease, due to decaying batteries within the resonance oscillator, progressively degrades the helium performance. This is particularly noticable between 2000 and 2100 when the pumping light intensity was increased to improve the signal-to-noise ratio. Note that the quality of system operation approaches that of the rubidium magnetometer in the period 1610-1700, although the minor perturbations within this period may not have affected each magnetometer. Disregarding the man-made disturbances, the helium tracking was within $\pm$ 3 gamma of the commercial magnetometer over the 45 gamma change which required 4 hours to record.

The third recording, Fig. 21, shows the relative system tracking ability for major field changes which occurred over short periods of time. The difference in scales is attributed to the recording equipment. In general, the helium system was within 0 5 gamma of the commercial magnetometer over short periods of time.

The fourth recording pair, Figs. 22 and 23, show a large perturbation in the field. Again the scale discrepancy is in the recording equipment. It is noteworthy that many minor field perturbations of the order of a few tenths of a gamma were recorded simultaneously by the magnetometers.

From the graphs obtained, it can be concluded that the helium magnetometer was operating within 0.5 gamma of the commercial magnetometer over short periods of time, (several minutes) and under optimum conditions. Due to drifting characteristics caused by battery decay, no approximation can be made for long-term accuracy, although the diurnal correlations prove tracking ability.

Unfortunately, the term "optimum", as used in this section, means "optimum considering the circumstances and environment"; and therefore, the true accuracy under conditions similar to the commercial magnetometer environment cannot be determined from the data obtained.

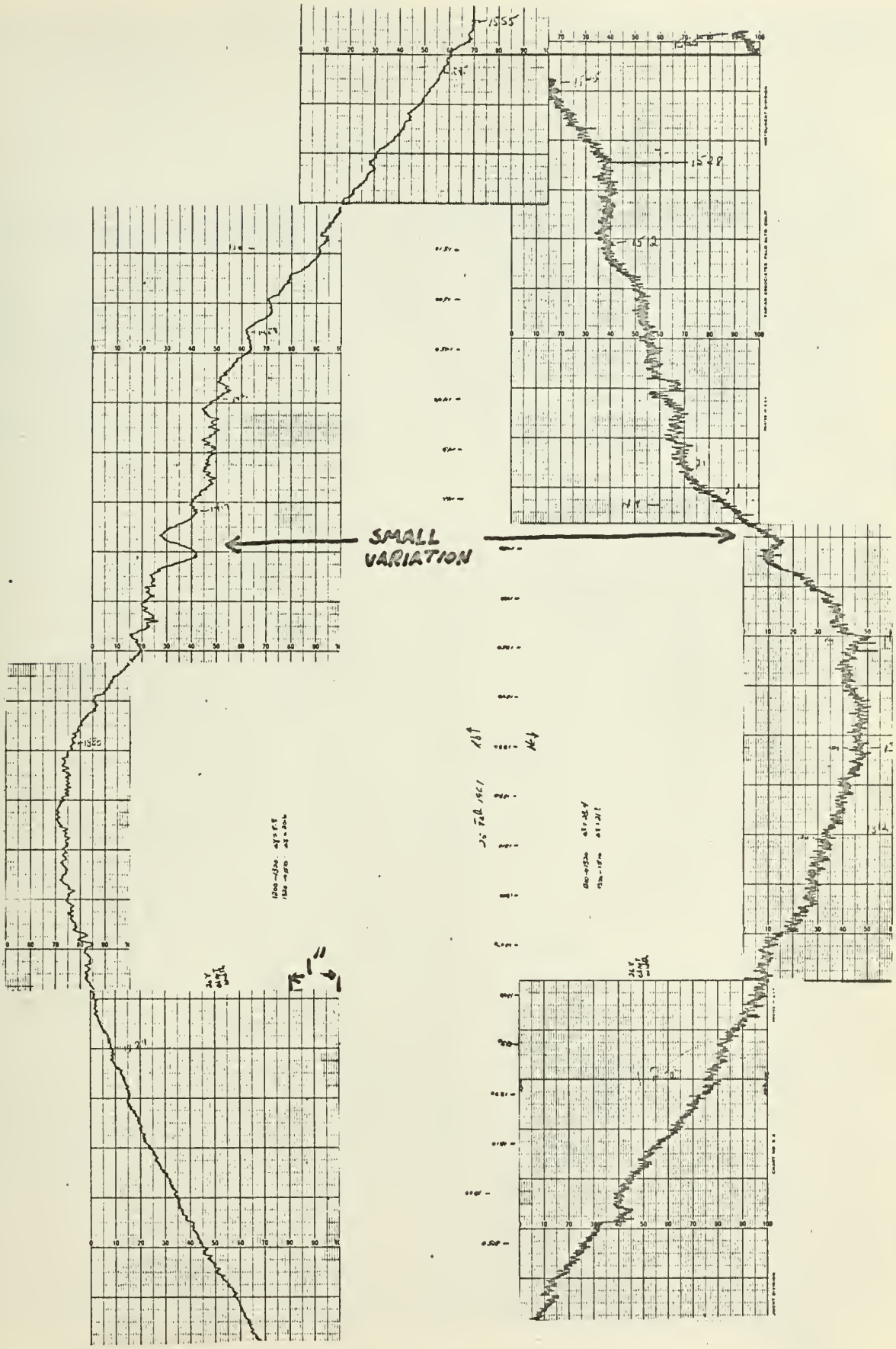

Fig. 19 System Performance- 27 February, 1961

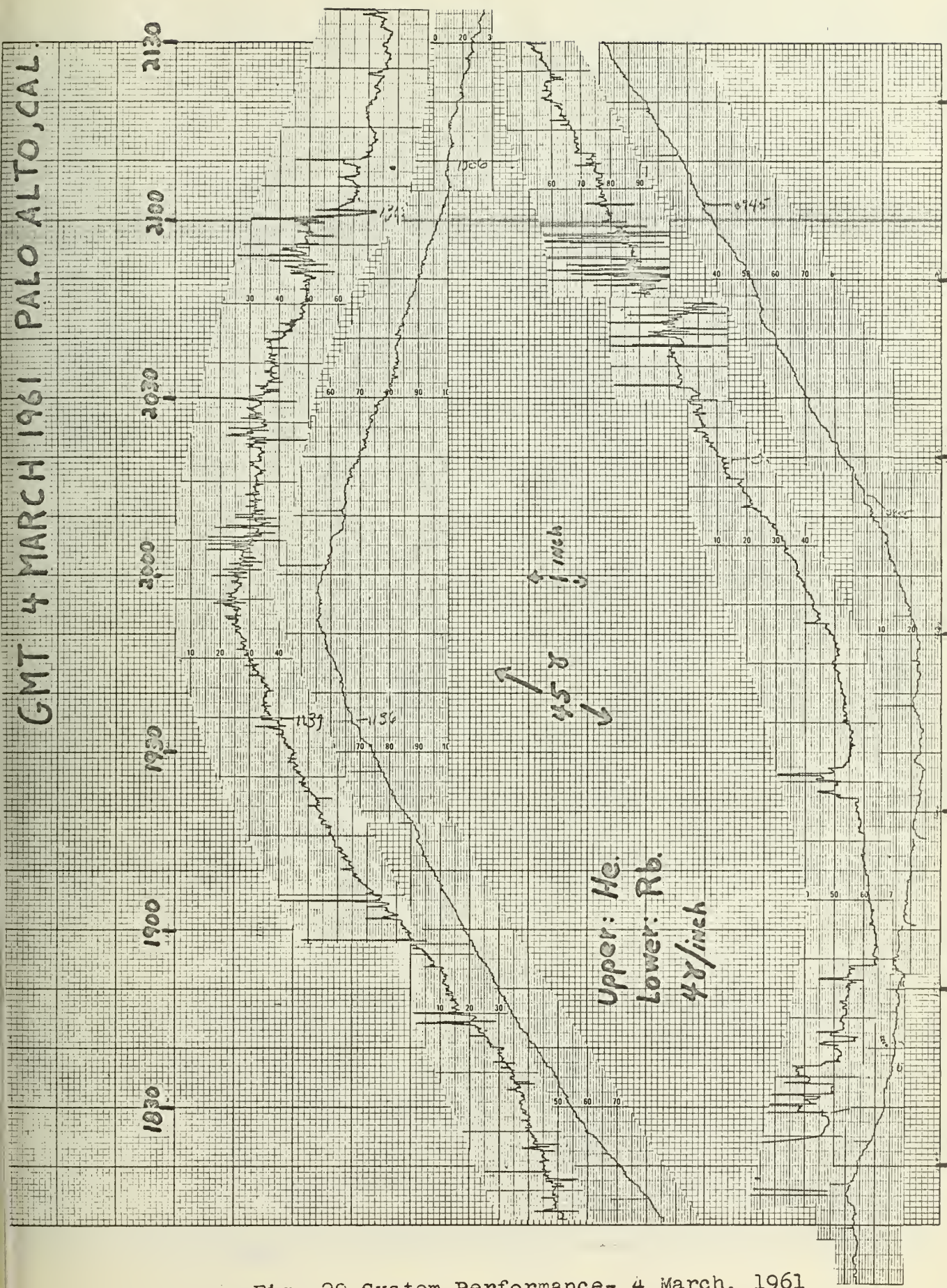

Fig. 20 System Performance- 4 March, 1961

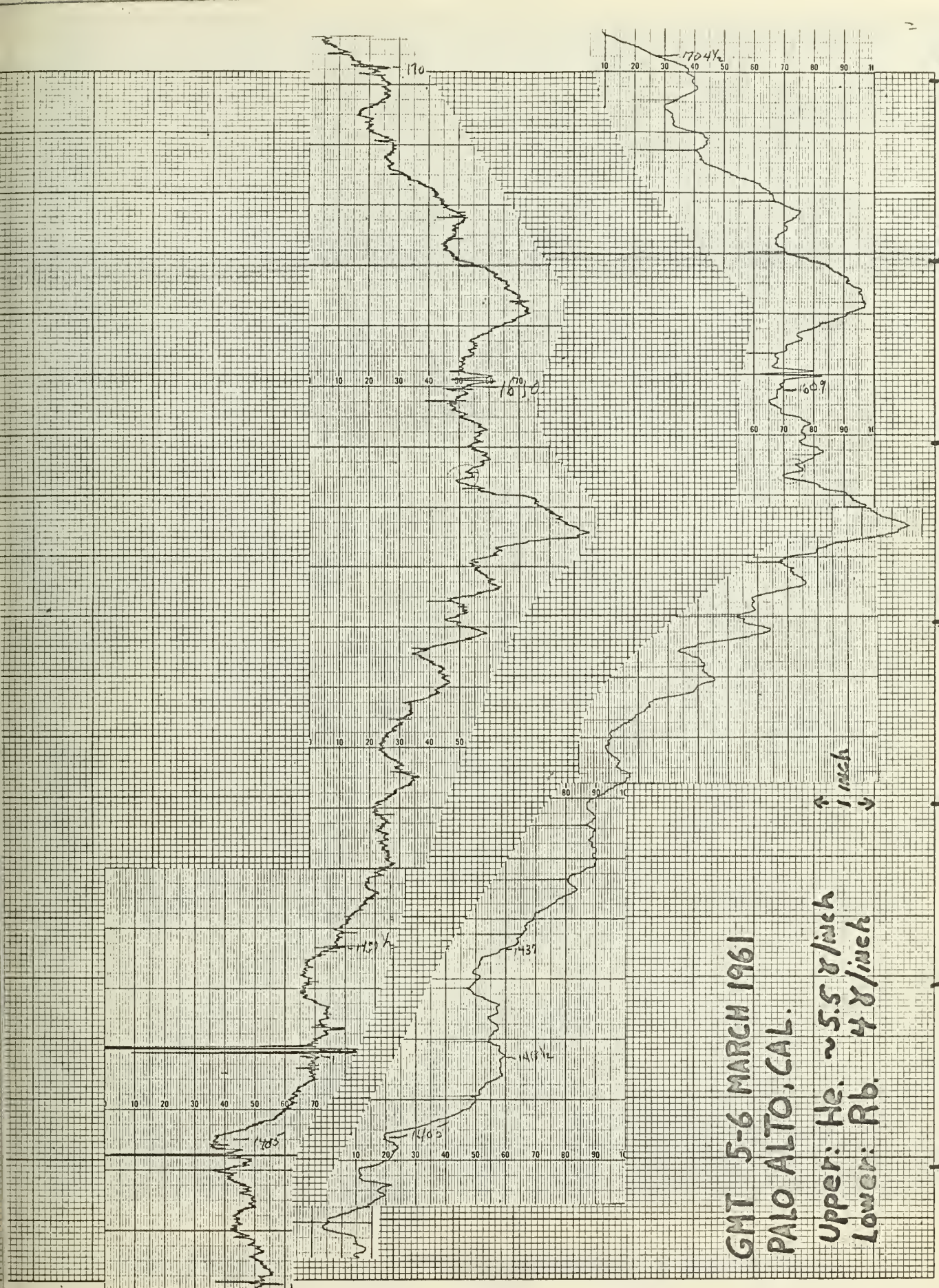

Fig. 21 System Performance 5-6 March 1961

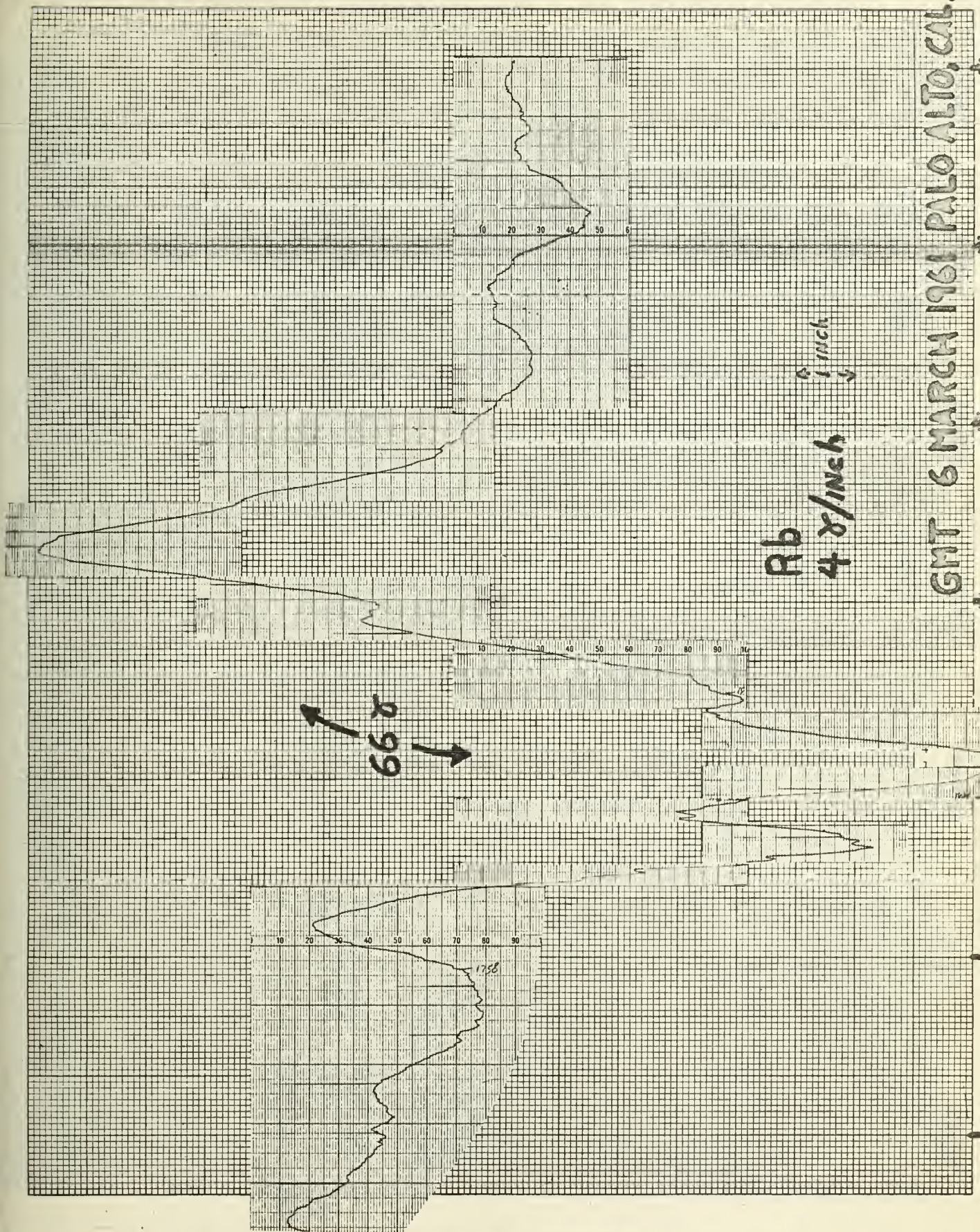

Fig. 22 Large Field Perturbation-Rubidium Magnetometer
6 March, 1961

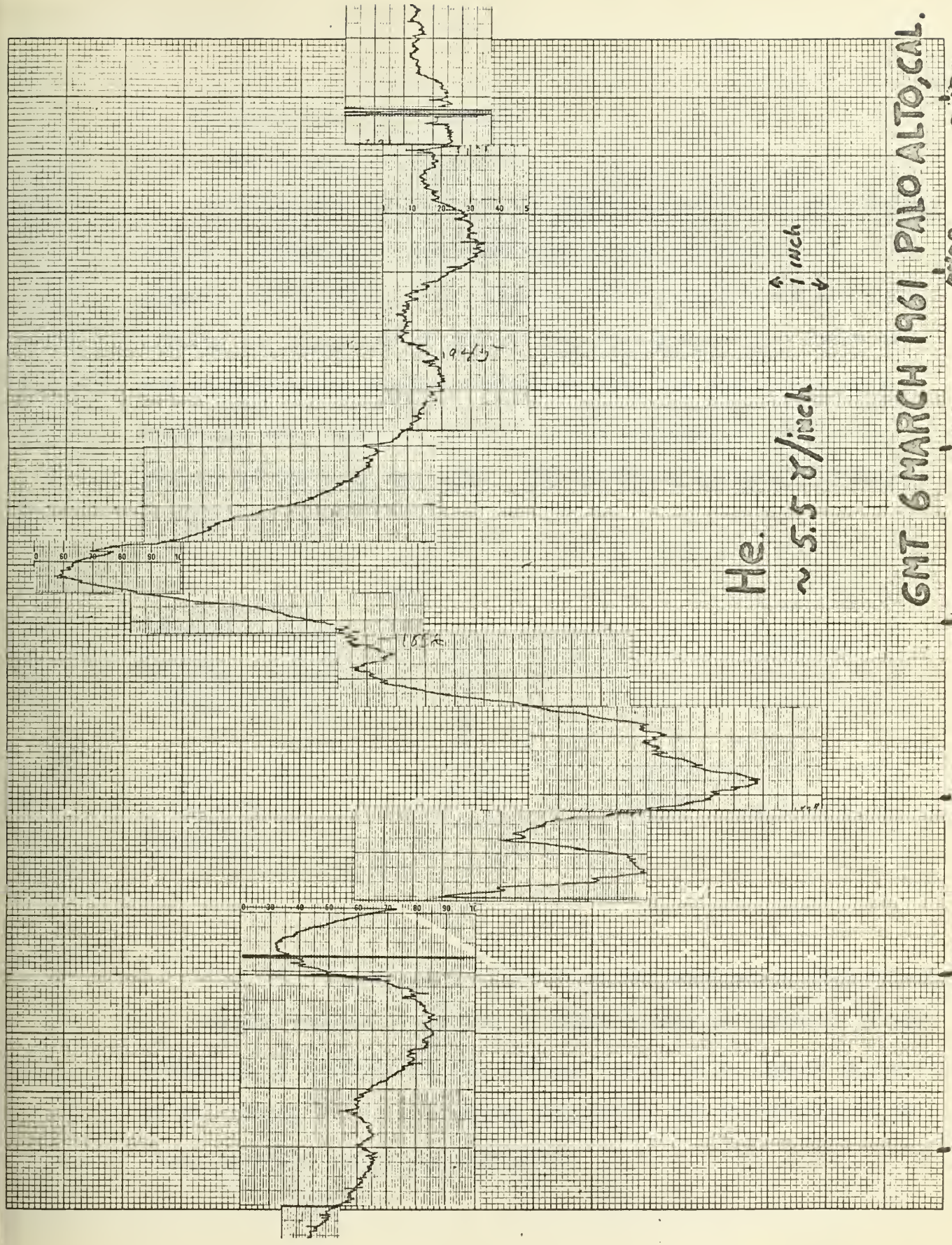

Fig. 23 Large Field Perturbation- Helium Magnetometer
6 March, 1961

B. The Subsidiary Measurements

1. The Absorption Phenomena

Although the analysis of the system operation is not dependent on a knowledge of the magnitude of the absorption, it is a graphic verification of the theory. To obtain information concerning the magnitude of absorption, photographs were taken of the photodetector voltage variations when the absorption cell discharge was turned on and off in the presence of and in the absence of the pumping light. The following equipment configuration was used:

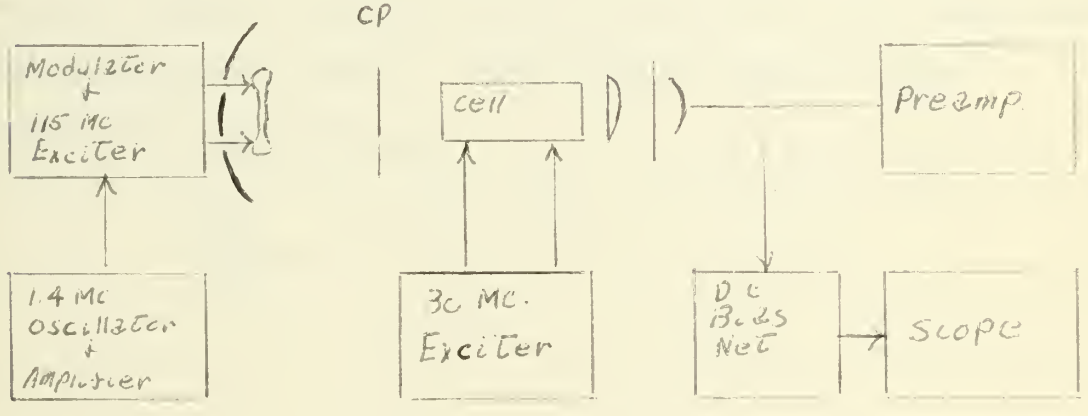

Fig. 24. Equipment Configuration for Absorption Observation

In the figures to follow, a light intensity increase is recorded as an increase in the voltage traces (i.e. upward deflection of the trace) and slow-changing transients are attributed to RC charging times within the equipment.

In Fig. 25 an increase in the light intensity at the detector was recorded when the pumping light remained on and the cell discharge was turned off. The magnitude of the change is approximately 600 millivolts with a detector bias of 38 volts. This is a 1.6% increase.

Fig. 26 shows a decrease in the light intensity at the detector when the pumping light remains off and the cell discharge is turned off. The magnitude of this change is approximately 50 millivolts or a 0.1% decrease.

The signal under these conditions is shown in Fig. 27. The measured signal-to-noise ratio was four, and the peak amplitude was approximately 600 uv. The resulting signal-to-light absorbed is approximately:

$$\frac{600}{\sim 5} \times 10^{-5} \cong 1 \times 10^{-3}$$

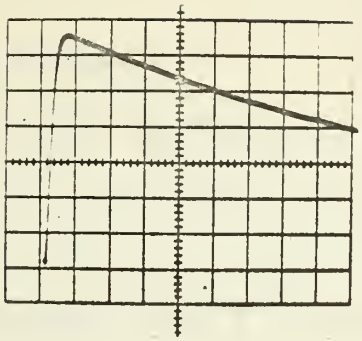

Fig. 25 Detector Voltage Variation-Lamp on, Cell off.
Scale: 0.1 volt/div, 10 msec/div

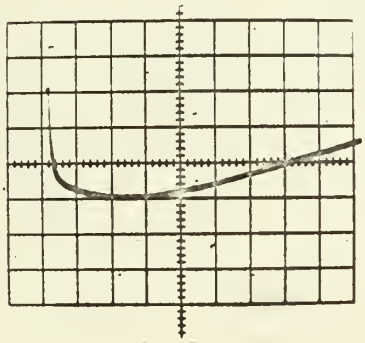

Fig. 26 Detector Voltage Variation-Lamp off, Cell off.
Scale: 0.02 volt/div, 10 msec/div.

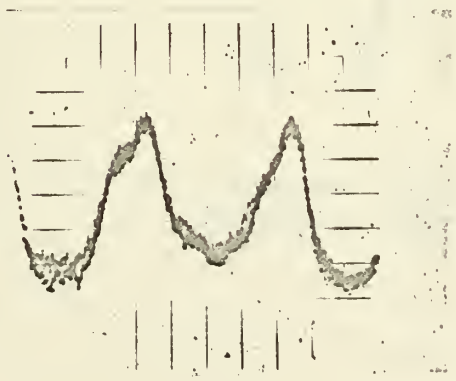

Fig. 27 The Unprocessed Signal. Scale: 50 mv/div
2 msec/div.

2. The Signal Processing

The average signal obtained in the 33 degree orientation is shown in Fig. 28. The signal-to-noise ratio was measured to be seven. By filtering to a 100-240 cycle bandwidth, a considerable improvement could be achieved as shown in Fig. 29 as a Lissajous and Fig. 30 on a linear sweep.

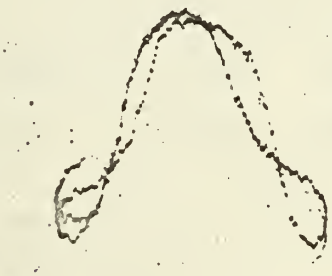

Fig. 28 Unprocessed Signal
S/N 7

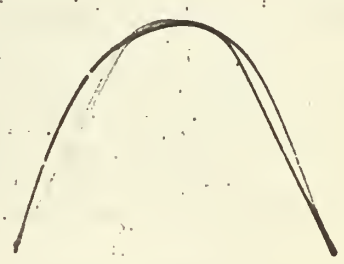

Fig. 29 Filtered Signal
Bandwidth 100-240 cps

Fig. 30 Processed Signal
Bandwidth 100-240 cps

3. The Measurement of Line Width

The signal entering the phase detector is symmetric in time only when the precession frequency coincides with the resonance oscillator frequency. This frequency corresponds to the ambient magnetic field. As the resonance oscillator is changed from this "correct" frequency, the phase detector will develop an error voltage which has a polarity determined by the direction of frequency change. The magnitude of the error voltage will continue to increase until the frequency error reaches one-half the line width, at which point the servo-system locking will become unstable. By use of a frequency counter, these points were measured under several representative sweep field conditions. The results were averaged to give an order-of-magnitude line width of approximately 10,000 cps.

VI. Conclusions

A. System Performance

The objective of this work has been to show that a modulated light helium magnetometer could be constructed and could be caused to follow the changes in the earth's magnetic field. During this endeavor, no particular value was placed on accuracy, per se, provided the resulting performance could be clearly associated with changes in the ambient field. The actual performance confirmed the fact that the system met this specification. During short periods of time, the performance of the system was within 0.5 gamma of the rubidium magnetometer.

Several modifications could be made to improve the accuracy of the experimental model:

1. Orientation:

The orientation used was such that only 30% of the theoretical maximum signal amplitude was obtained. By obtaining the maximum signal amplitude, a three-fold increase in signal-to-noise ratio could be expected.

2. Environment

The experimental equipment was installed in a building which contained a variable 60 cycle sweep field and equipment which caused magnetic interference. These factors were noted to cause as much as two gamma shifts in the recorded output together with additional noise perturbations. A magnetically-clean environment could eliminate these problems.

3. Packaging

The system components used were bulky and, for the most part, inadequately shielded. This added to the "magnetic-clutter" previously mentioned under environment, and it also provided numerous sources of noise. By designing equipment specifically for the system, a general improvement in performance could be expected.

4. Line Width

The line width directly effects the accuracy of the system. Magnetic field homogeneity in the absorption cell will determine the line width for a given operating condition. The line width measured in the present case was approximately 10,000 cps, which is considerably more than one might estimate from a theoretical value. An effort to clean up the magnetic environment and the addition of a homogeneous magnetic sweep would result in greater system accuracy.

5. Reference Crystal Oscillator

The recording system accuracy is dependent on the accuracy of the reference crystal oscillator, the frequency meter and the recording equipment. In the present case, a crystal reference oscillator was used which contained no shielding from other equipment and no temperature stabilization. By using a reference system which has a short term stability of one part in a million, a .05 gamma error would be present which could not be improved by changes in the magnetometer. The inaccuracies of the frequency meter and the recording equipment further degrade the recorded performance.

With the above modifications, the experimental performance could be expected to improve. With sufficient care, the accuracy of the system could conceivably approach the limitations imposed by the reference oscillator.

BIBLIOGRAPHY

1. Proceedings of the Ann Arbor Conference on Optical Pumping, University of Michigan, 1959.

2. F. D. Colgrove and P. A. Franken, Optical Pumping of Helium in the $^3S_1$ Metastable State, Phys. Rev. 119, 680 (1960).

3. W. E. Bell and A. L. Bloom, Optically Driven Spin Precession, Phys. Rev. Ltrs 6, 280, March 15, 1961.

4. G. Herzberg, Atomic Spectra and Atomic Structure, Dover Publications, 1944.

5. J. R. Singer, Masers, Wiley & Sons, 1959.

6. A. Kastler, Proc. Phys. Soc., A67,853 (1954)

7. W. B. Hawkins, Orientation and Alignment of Sodium Atoms by means of Polarized Resonance Radiation, Phys. Rev. 98, 478, (1955).

8. F. Bloch, Nuclear Induction, Phys. Rev. 70, 460, (1946)

9. W. E. Bell and A. L. Bloom, Optical Detection of Magnetic Resonance in Alkali Metal Vapor, Phys. Rev. 107, 1559 (1957).

APPENDIX A

ZEEMAN LEVEL ENERGY CONSIDERATIONS

From classical mechanics, the force exerted on a magnetic monopole is given by:

$$F = mH$$

Where: m = magnetic charge

H = magnetic field intensity

The torque acting on a pivoted monopole will be:

$$T = \ell F \sin\theta$$
$$= \ell m H \sin\theta$$

Where: ℓ = length of the pivot arm.

θ = angle between the monopole axis and the field.

But, ℓm is simply the magnetic moment, μ so:

$$T = \mu H \sin\theta$$

The Energy associated with this torque is:

$$E = \int_{\frac{\pi}{2}}^{\theta} T\, d\theta = -\mu H \cos\theta \qquad (1)$$

where $E = 0$ corresponds to the field-free condition.

Let L be the net angular momentum. Then, for a charge, q, moving in a circular orbit at angular rate ω :

$$L = m r^2 \omega$$

But,

$$\mu = i A$$
$$= \frac{qA}{T}$$
$$= q f A$$

where i = the filamentary current established by the rotating charge.

T = period of orbit. = $\frac{1}{f}$

A = area of orbit.

Hence:

$$\mu = \frac{LB}{2m}$$

Expressing the charge in electrostatic units and combining these results for an electron:

$$\bar{\mu} = \frac{-e\bar{L}}{2mc} \tag{2}$$

The angular orbital momentum of the electron is:

$$\frac{h}{2\pi}\sqrt{L(L+1)} \tag{3}$$

and that of the spin has been found to be twice that of (3):

$$\frac{2h}{2\pi}\sqrt{S(S+1)} \tag{4}$$

Combining (3) and (4) into (2):

$$\bar{\mu}_L = \frac{-eh}{4\pi mc}\sqrt{L(L+1)}\,\bar{a}_L = -\mu_B\sqrt{L(L+1)}\,\bar{a}_L \tag{5}$$

$$\bar{\mu}_S = \frac{-2eh}{4\pi mc}\sqrt{S(S+1)}\,\bar{a}_S = -2\mu_B\sqrt{S(S+1)}\,\bar{a}_S \tag{6}$$

where μ_B = Bohr magneton = 0.9273×10^{-20} erg/oersted.

Drawing these results in vector form:

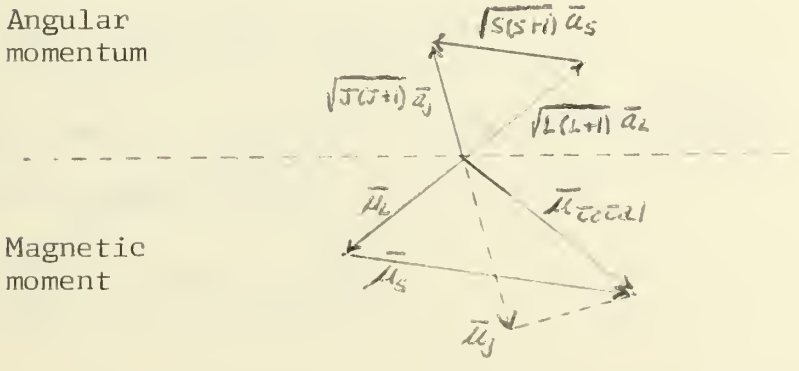

Fig.31. Vector sum of the Moments and Momenta.

It can be noted that where spin is involved the net angular momentum vector is not aligned with the net magnetic moment. The component of the net magnetic moment which is then of interest can be calculated:

$$\mu_J = \mu_L \cos[\mu_L, \mu_J] + \mu_S \cos[\mu_S, \mu_J] \tag{7}$$

But from the law of cosines:

$$\cos[\mu_L, \mu_J] = \frac{J(J+1) + L(L+1) - S(S+1)}{2\sqrt{J(J+1)}\,L(L+1)} \tag{8}$$

$$\cos[\mu_S, \mu_J] = \frac{S(S+1) + J(J+1) - L(L+1)}{2\sqrt{J(J+1)}\,S(S+1)} \tag{9}$$

and combining (5) through (9):

$$\frac{-\mu_J}{\mu_B} = \left\{\frac{3}{2} + \frac{S(S+1) - L(L+1)}{2J(J+1)}\right\}\sqrt{J(J+1)} = g\sqrt{J(J+1)} \tag{10}$$

where g is the Lande g-factor.

Combining (1) and (10):

$$E = g\mu_B\sqrt{J(J+1)}\,H\cos\theta \tag{11}$$

which can be expressed in terms of the $\sqrt{J(J+1)}$ projection on the magnetic axis:

$$\Delta E = g\mu_B H(\Delta M) \tag{12}$$

where: $M = \sqrt{J(J+1)}\cos\theta$

APPENDIX B

THE EFFECT OF POLARIZATION ON TRANSITIONS

The intensity of radiation from the atom is dependent on the magnitude of the change in the dipole moment. In the case of two charges ϵ and $-\epsilon$ positioned a distance d from each other, the dipole moment is a vector of magnitude ϵd . In an ensemble of point charges, the dipole moment vector could be defined by the cartesian components:

$$\sum_i \epsilon_i x_i \qquad \sum_i \epsilon_i y_i \qquad \sum_i \epsilon_i z_i$$

In the case of a single point charge whose exact position is unknown, a certain fraction of the total charge ϵ can reasonably be considered to be at a fixed point if the distribution probability is known. Since the probability density function is $\psi \psi^*$, from quantum mechanics, the electric density would be:

$$\rho = \epsilon \psi \psi^*$$

and the electric dipole moment components for a single electron would be:

$$P_x = \int \epsilon \psi_n \psi_n^* x \, d\tau \tag{1}$$

$$P_y = \int \epsilon \psi_n \psi_n^* y \, d\tau \tag{2}$$

$$P_z = \int \epsilon \psi_n \psi_n^* z \, d\tau \tag{3}$$

where $d\tau$ is the element of volume and the subscript represents the stationary state n .

If the transition from state n to state m is made, the electric moment (transition moment) $\bar{P}$ can be described by the same equations with the change $\psi_m \psi_m^*$ for $\psi_n \psi_n^*$.

It may be recalled that the Schrodinger equation can be written:

$$\frac{-h^2}{8\pi^2 m}\left[\frac{\partial^2 \Psi}{\partial x^2}+\frac{\partial^2 \Psi}{\partial y^2}+\frac{\partial^2 \Psi}{\partial z^2}\right]+V\Psi=\frac{jh}{2\pi}\frac{\partial \Psi}{\partial t}$$

which has a solution:

$$\Psi = \psi e^{-j2\pi\left(\frac{E}{h}\right)t} \tag{4}$$

where: ψ is the time independent solution.

E = Energy
t = time
h = Planck's constant

Considering the time factor solution applied to the two states, results in:

$$e^{-j2\pi\left[\frac{E_n - E_m}{h}\right]t} \tag{5}$$

where there exists the familiar relation that the energy difference is related to the frequency by:

$$f = \frac{E_n - E_m}{h}$$

If $\bar{R}^{nm}$ is a vector which defines the amplitude of the vibration of the electric moment, $\bar{P}^{nm}$ then the combination of (1), (2), (3) and (5) results in:

$$\bar{P}^{nm} = \epsilon \bar{R}^{nm} e^{-j2\pi\left[\frac{E_n - E_m}{h}\right]t}$$

as the time-variable electric moment associated with the transition n to m. $\bar{R}^{nm}$ has the components:

$$R_x^{nm} = \int \psi_n \psi_m x \, d\tau \quad , \quad etc. \tag{6}$$

Considering a magnetic field direction along the Z axis, the characteristic solutions to the Schrodinger equation would take the form:

$$\psi_n = f e^{j m_f \phi} \qquad \psi_m = g e^{j m_g \phi} \tag{7}$$

since the states are rotationally symmetric about the magnetic field.

Combining (6) and (7):

$$R_x^{nm} = \iint f g^* e^{j(m_f - m_g)\phi} x \, d\tau$$

and similarly for Y and Z.

In cylindrical coordinates:

$$d\tau = \rho \, d\phi \, d\rho \, dz$$
$$x = \rho \cos \phi$$
$$y = \rho \sin \phi$$

The Z component of $\bar{R}^{nm}$ is then:

$$R_z^{nm} = \iiint f g^* e^{j(\Delta m)\phi} z \rho \, d\phi \, d\rho \, dz$$
$$= \iint f g^* z \rho \, dz \, d\rho \int e^{j(\Delta m)\phi} d\phi$$

where: $\Delta m = m_f - m_g$

This integral is non-zero only when:

$$\int_0^{2\pi} e^{j(\Delta m)\phi} d\phi \qquad \text{is non-zero.}$$

An examination of this latter integral will reveal that the result will not be zero if: $\Delta m = 0$

This, of course, indicates that only those transitions involving $\Delta m = 0$ can occur parallel to the magnetic field.

The x component of $\bar{R}^{nm}$ is:

$$R_x^{nm} = \iint f g^* \rho^2 \, dz \, d\rho \int e^{j(\Delta m)\phi} \cos\phi \, d\phi$$

where the latter integral can be written:

$$\frac{1}{2} \int \left[e^{j(\Delta m + 1)\phi} + e^{j(\Delta m - 1)\phi} \right] d\phi$$

This has a non-zero value only if $\Delta m = \pm 1$. Similarly, for the y component:

$$\frac{1}{2j} \int \left[e^{j(\Delta m + 1)\phi} - e^{j(\Delta m - 1)\phi} \right] d\phi$$

Now let $\Delta m = -1$. Examining the ϕ dependence of the x component:

$$R_x^{nm} = F(\rho, z) \int e^{j \Delta m \phi} d\phi = F(\rho, z)\pi$$

The y component is:

$$R_y^{nm} = -j \, G(\rho, z)\pi$$

Hence, the vector $\bar{R}^{nm}$ is:

$$\bar{R}^{nm} = F(\rho, z)\pi \, \bar{a}_x - j \, G(\rho, z)\pi \, \bar{a}_y$$

Looking into the Z axis, the y component lags behind the x component by 90 degrees in time, and the rotation is counterclockwise. An investigation of $\Delta m = +1$ will reveal a circular polarization of opposite direction.

APPENDIX C

THE POPULATION DENSITY CONSIDERATIONS

As described previously, the general pumping action is an absorption process which effectively excites the individual atom from a ^3S sublevel to a ^3P sublevel. Each allowed transition has a finite relative probability of occurrence which can be calculated[10], but the need does not arise here. The allowed downward transitions can be assumed to be primarily due to the spontaneous emission.

In the case of gas pressures in the order of a few millimeters or higher, there is a considerable disorientation and loss of phase memory in the ^3P levels before the downward transitions can occur. This allows the simplifying assumption, often used, that all the ^3S sublevels have an equal probability of being repopulated by the returning atoms.(2) (9) In the present case, however, the gas pressure is in the order of one-half millimeter, and it must be assumed that no such disorientation exists.

The primary interest here is to show that an orientation can exist by virtue of a net population increase of one ^3S sublevel at the expense of the other two in the absence of thermal relaxation effects.

The allowed helium transitions which are of interest are shown in Fig. 32.

[10]Condon and Shortley, The Theory of Atomic Spectra, Cambridge Press, 1935, Chap. 3.

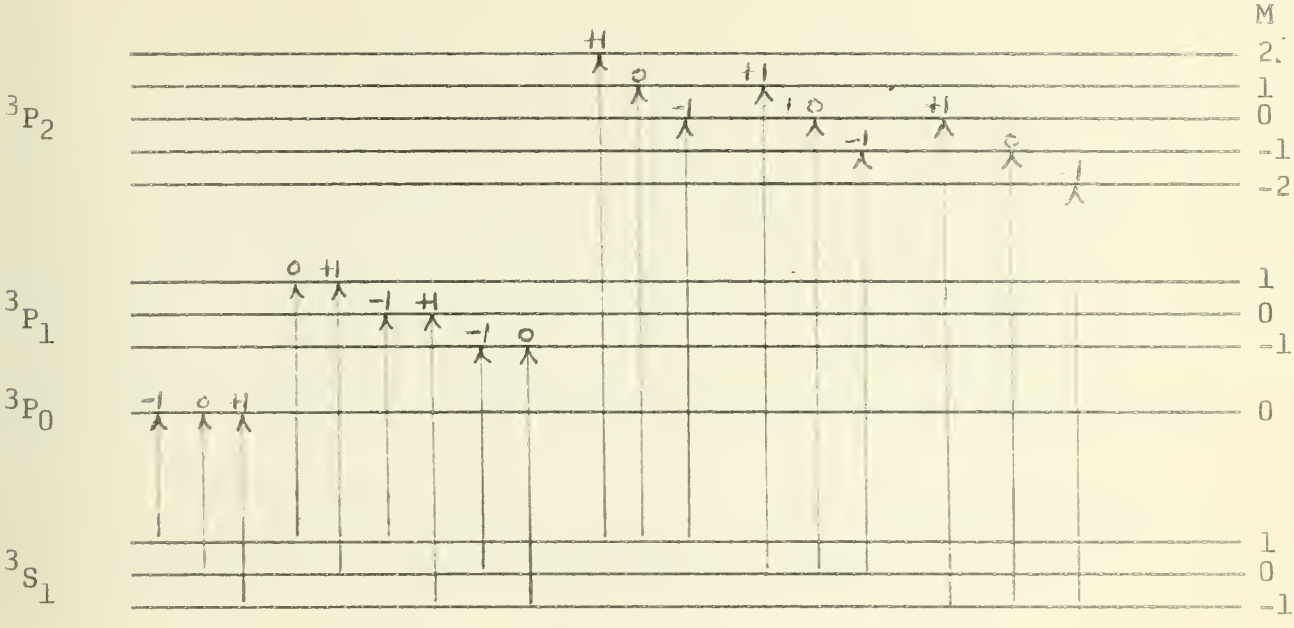

Fig. 32. The Allowed Transitionsin Helium

A table of upward-going transition rates can be formed:

	$^3P_0$		$^3P_1$		$^3P_2$				
ΔM	0	1	0	-1	2	1	0	-1	-2
$^3S_1$ +1	$^0R_+^0$	$^1R_+^1$	$^1R_+^0$	0	$^2R_+^2$	$^2R_+^1$	$^2R_+^0$	0	0
0	$^0R_0^0$	$^1R_0^1$	0	$^1R_0^{-1}$	0	$^2R_0^1$	$^2R_0^0$	$^2R_0^{-1}$	0
-1	$^0R_-^0$	0	$^1R_-^0$	$^1R_-^{-1}$	0	0	$^2R_-^0$	$^2R_-^{-1}$	$^2R_-^{-2}$

Table 1. Absorption Transition Rates

Only the circled values will be allowed with circularly polarized light in accordance with Appendix B, where $\Delta M = +1$.

The relative spontaneous emission probabilities have been computed by Colgrove and Franken (2) :

	$^3P_0$		$^3P_1$			$^3P_2$				
M	0	1	0	-1	2	1	0	-1	-2
+1	2	3	3	0	6	3	1	0	0
0	2	3	0	3	0	3	4	3	0
-1	2	0	3	3	0	0	1	3	6

$^3S_1$

Table 2. Relative Spontaneous Emission Probabilities

Comparing these two tables, a tabulation can be made to replace Table 2 when using polarized light:

	$^3P_0$	$^3P_1$			$^3P_2$				
M	0	1	0	-1	2	1	0	-1	-2
+1	$\frac{1}{3}{}^0R^0_-$	$\frac{1}{2}{}^1R^1_0$	$\frac{1}{2}{}^1R^0_-$	0	${}^2R^2_+$	$\frac{1}{2}{}^2R^1_0$	$\frac{1}{6}{}^2R^0_-$	0	0
0	$\frac{1}{3}{}^0R^0_-$	$\frac{1}{2}{}^1R^1_0$	0	0	0	$\frac{1}{2}{}^2R^1_0$	$\frac{2}{3}{}^2R^0_-$	0	0
-1	$\frac{1}{3}{}^0R^0_-$	0	$\frac{1}{2}{}^1R^0_-$	0	0	0	$\frac{1}{6}{}^2R^0_-$	0	0

$^3S_1$

Table 3. Spontaneous Emission Probabilities in terms of Absorption Rates

The rate equations which describe the change in population densities may now be written. Let CR_+ give the absolute absorption rate for the ^3S, +1 level, etc. Then:

$$\frac{1}{c}\frac{dn_+}{dt} = n_+\left[{}^2R^2_+ - {}^2R^2_+\right] + n_0\left[\tfrac{1}{2}{}^2R^1_0 + \tfrac{1}{2}{}^1R^1_0\right] + n_-\left[\tfrac{1}{6}{}^2R^0_- + \tfrac{1}{2}{}^1R^0_- + \tfrac{1}{3}{}^0R^0_-\right]$$

$$\frac{1}{c}\frac{dn_0}{dt} = -n_0\left[\tfrac{1}{2}{}^2R^1_0 + \tfrac{1}{2}{}^1R^1_0\right] + n_-\left[\tfrac{2}{3}{}^2R^0_- + \tfrac{1}{3}{}^0R^0_-\right]$$

$$\frac{1}{c}\frac{dn_-}{dt} = -n_-\left[\tfrac{5}{6}{}^2R^0_- + \tfrac{1}{2}{}^1R^0_- + \tfrac{2}{3}{}^0R^0_-\right]$$

where n_+, n_0 and n_- denote the instantaneous sublevel populations and $N = n_+ + n_0 + n_-$.

Note that the atoms pumped from the +1 sublevel return to that level, whereas the other two levels are being depleted. Assuming equal pumping light intensities and no relaxation effects, the +1 sublevel population will become N.

APPENDIX D

THE EQUIPMENT SCHEMATIC DIAGRAMS

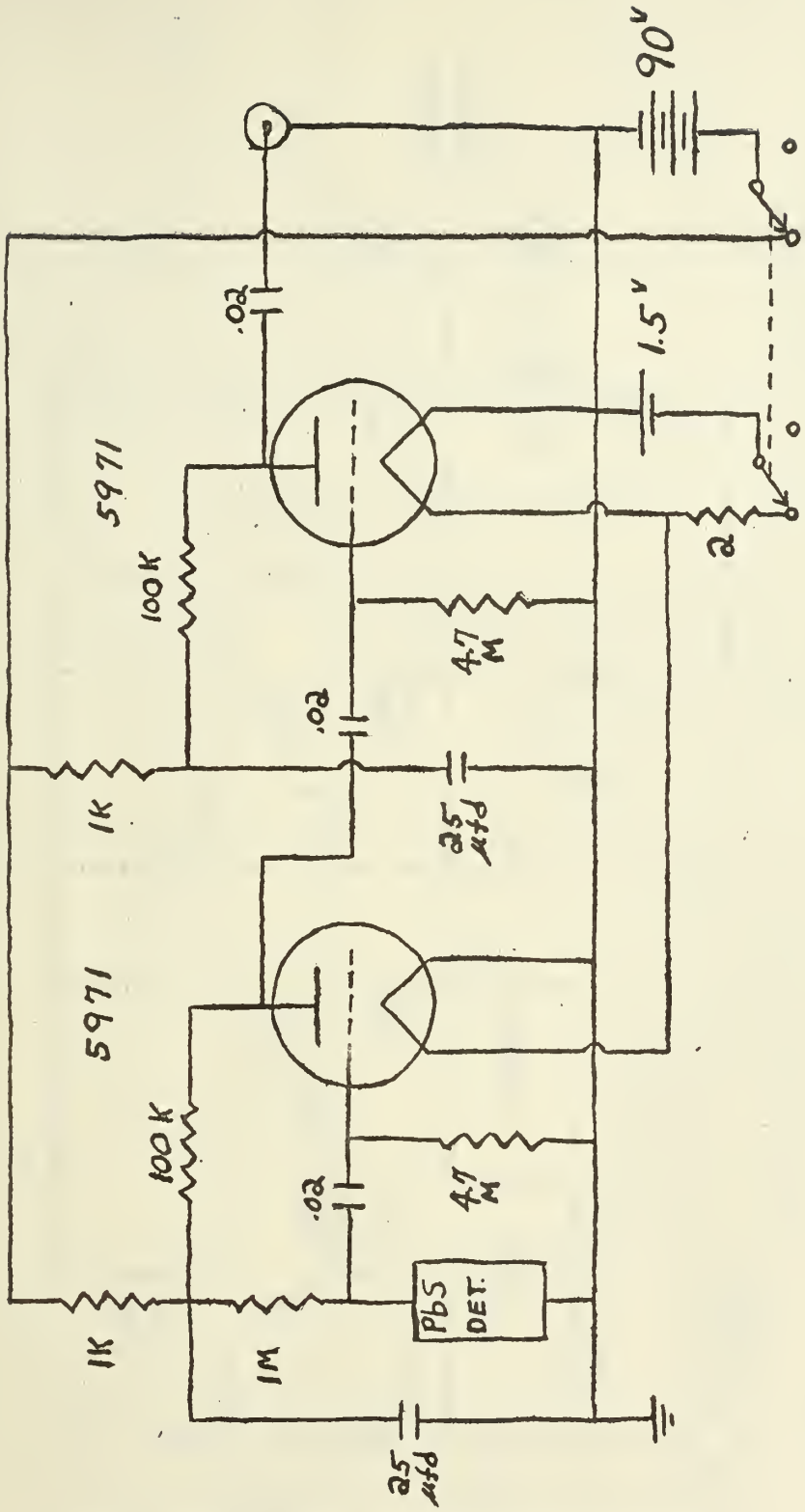

Diagram 1 Photodetector Preamplifier

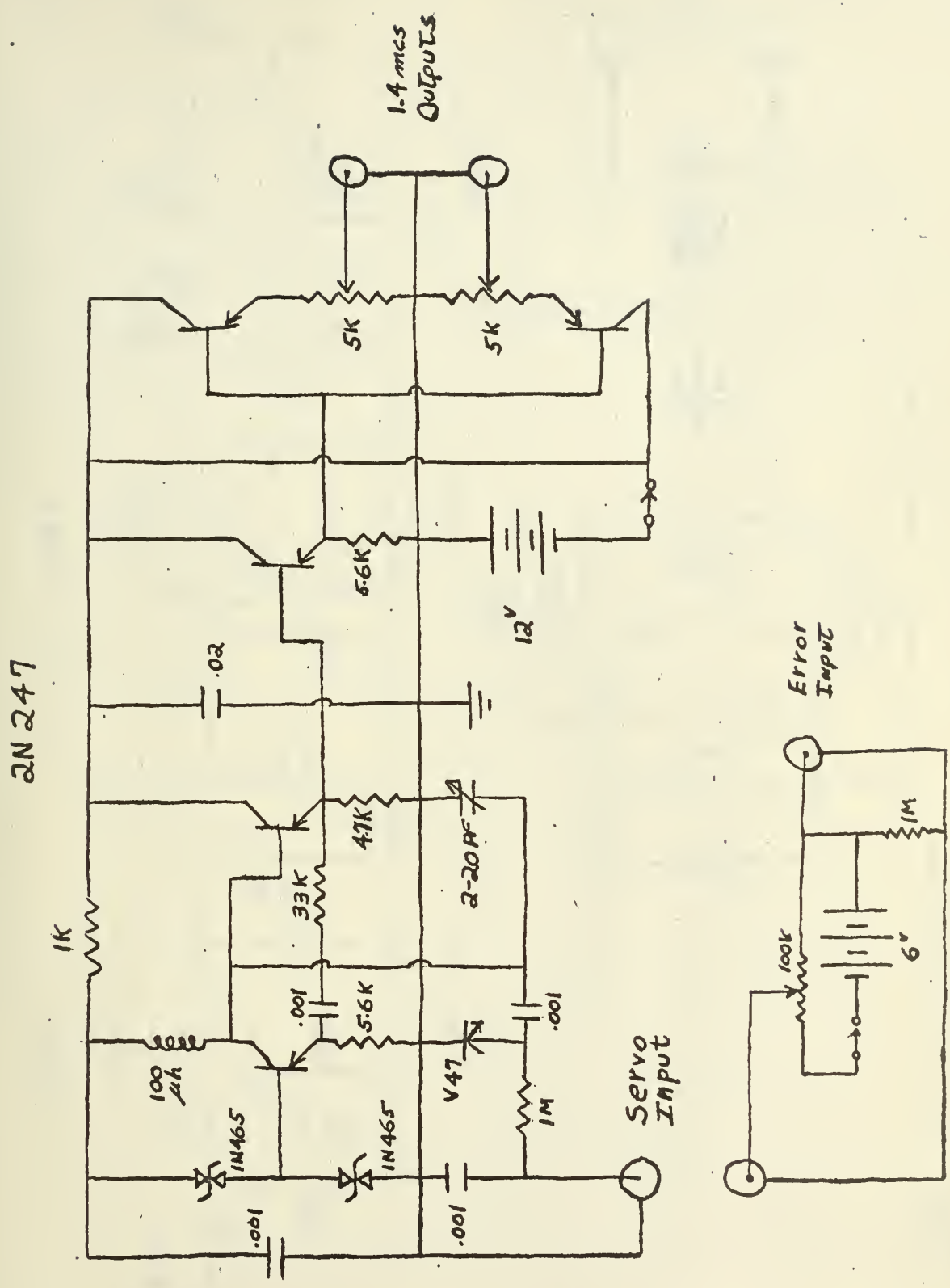

Diagram 2 1.4 mc. Oscillator and Frequency Control Unit

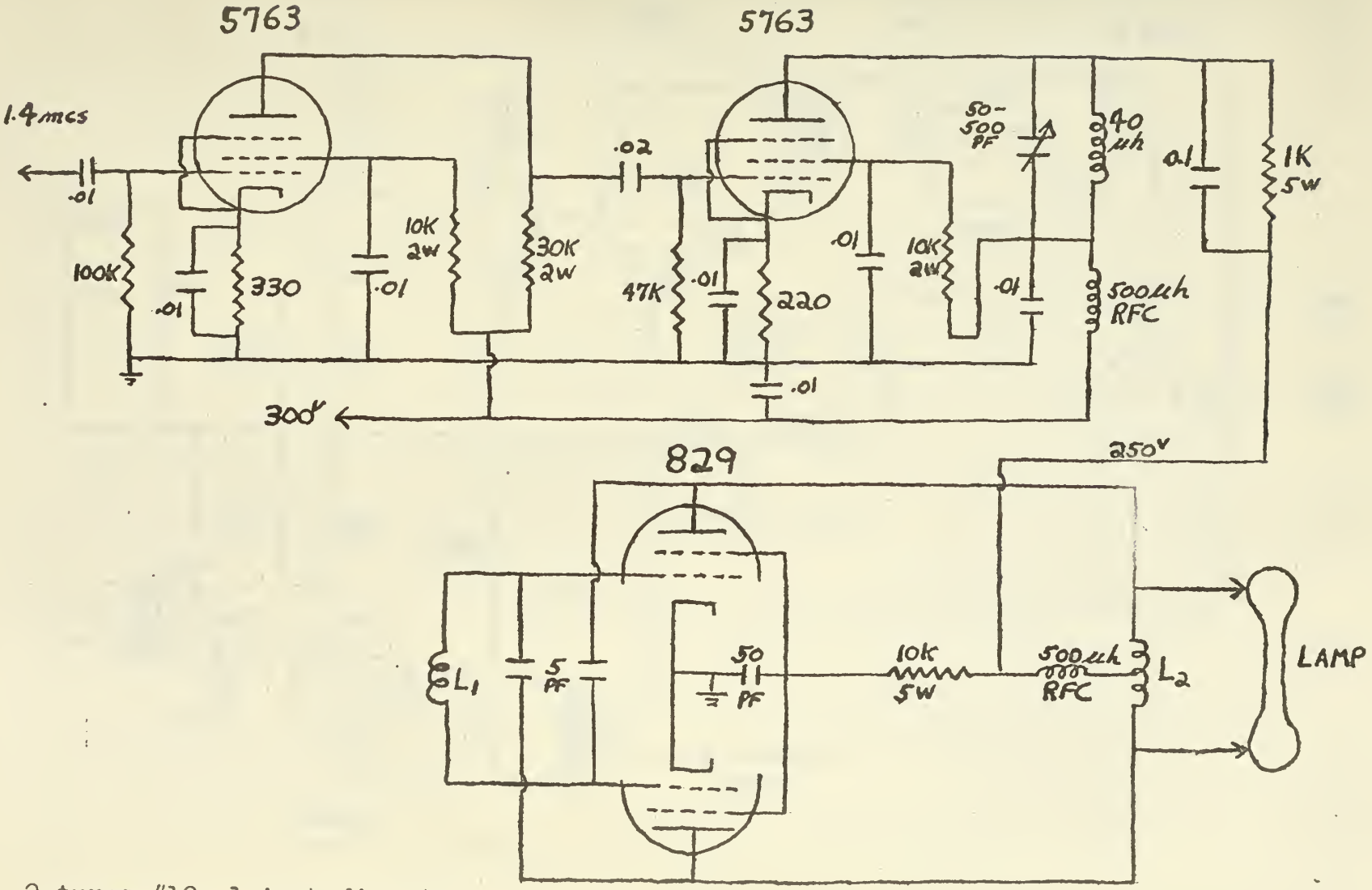

L_1 2 turns #12, 1 inch diameter; spacing- 2 wire diamters.

L_2 Same except 3 turns.

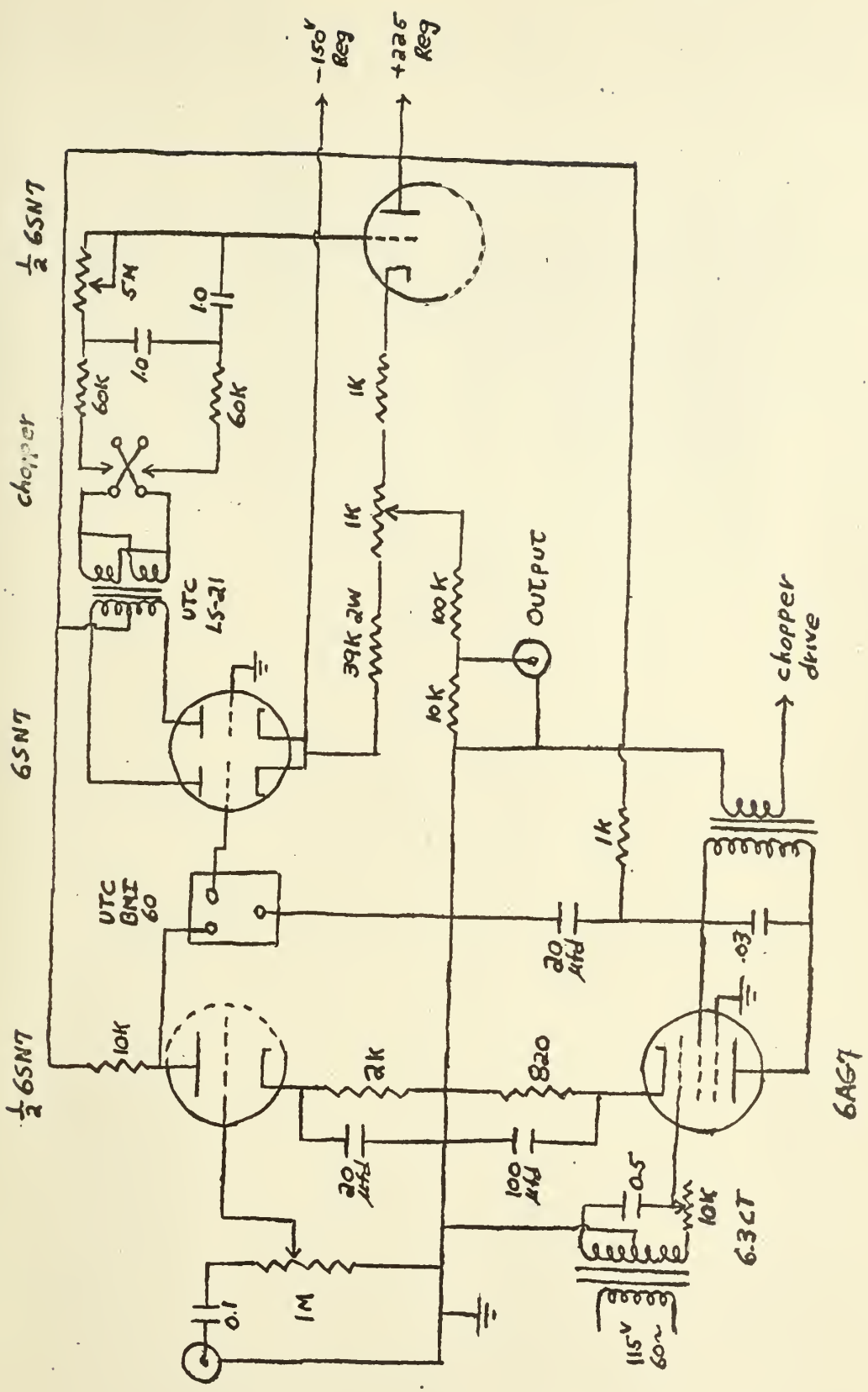

Diagram 4 60 cycle Phase Detector

MR 3 64
AG 3 1 61
BINDERY
INTERLIB
Texas Instruments
Thesis
50403
A36 Aldrich
A helium magnetometer that utilizes light-modulation.
JAN 19 1962
AEC - OAK RIDGE, Tenn.
NASA Goddard Space Flt Ctr
Greenbelt, Md.

Thesis
50403
A36 Aldrich
A helium magnetometer that utilizes light-modulation.

A helium magnetometer that utilizes ligh
3 2768 001 90978 1
DUDLEY KNOX LIBRARY